Check for updates

Small

NANO · MICRO small
www.small-journal.com

RESEARCH ARTICLE OPEN ACCESS

Deciphering Interfacial Electronic Interactions Between Iridium Oxide and Ni-Based Supports for High-Current-Density Anion Exchange Membrane Water Electrolysis

Yeongbin Lee[1] | Seohyeon Jang[2] | Seokjin Hong[3] | Seoyeon Jeong[2] | Ju Young Kim[1] | Wooseok Jeong[1] | Hyeonseok Lee[1] | Gyuhyeon Kim[1] | Hyungbin Son[1] | Sang Hyun Ahn[3] | Inho Nam[2] | Don-Hyung Ha[1]

[1]School of Integrative Engineering, Chung-Ang University, Seoul, Republic of Korea | [2]Department of Chemical Engineering, Department of Advanced Materials Engineering, Department of Intelligent Energy and Industry, Chung-Ang University, Seoul, Republic of Korea | [3]Department of Chemical Engineering, Chung-Ang University, Seoul, Republic of Korea

Correspondence: Sang Hyun Ahn (shahn@cau.ac.kr) | Inho Nam (inhonam@cau.ac.kr) | Don-Hyung Ha (dhha@cau.ac.kr)

Received: 22 December 2025 | **Revised:** 14 May 2026 | **Accepted:** 19 May 2026

Keywords: Anion exchange membrane water electrolyzer| Binder-free electrode| Catalyst–support interaction| Iridium oxide| Oxygen evolution reaction

ABSTRACT

Enhancing the oxygen evolution reaction (OER) performance of Ir-based catalysts while minimizing Ir usage is crucial for advancing anion exchange membrane water electrolyzers (AEMWEs). Herein, we present binder-free iridium oxide (IrO_2)-Ni-based electrodes prepared via a liquid-phase synthesis, which directly anchors an ultralow quantity of IrO_2 nanoparticles onto versatile Ni-based foams. This design enables systematic investigation of how Ni-based support chemistry modulates interfacial electronic interactions and thereby dictates catalytic performance. Electrochemical measurements reveal that IrO_2 on nickel phosphide (Ni_2P) exhibits the highest activity and durability, with a significantly low overpotential of 232 mV and stable operation over 400 h at 10 mA cm^{-2}. Spectroscopic and density functional theory (DFT) analyses reveal that strong interfacial charge transfer between IrO_2 and Ni_2P enriches the electron density around Ir and downshifts the Ir d-band center, thereby optimizing the adsorption energetics of OER intermediates and accelerating the reaction kinetics. The binder-free configuration enhances mechanical integrity and mass transport, which enables high-current-density operation (3.1 A cm^{-2} at 2.0 V_{cell}) under practical AEMWE conditions. Thus, the Ni-based support material enables tuning of the interfacial electronic coupling and catalytic behavior of IrO_2, thereby supporting the development of binder-free low Ir-loaded electrodes for cost-effective and durable AEMWEs.

1 | Introduction

The oxygen evolution reaction (OER) is a key half-reaction in water electrolysis, yet its sluggish kinetics require the electrocatalyst to be highly active and durable [1]. Iridium oxide (IrO_2) remains the benchmark OER catalyst in practical electrolyzer systems due to its exceptional structural robustness and corrosion resistance [2, 3]. However, the scarcity and high cost of Ir, along with its lower intrinsic activity compared to RuO_2, highlight the need for innovative strategies that drastically enhance the catalytic efficiency of IrO_2 while maximizing Ir utilization [4, 5].

Beyond intrinsic activity, another significant bottleneck arises from the conventional fabrication of Ir-based electrodes is caused by mixing catalyst powders with polymeric binders and conductive additives before coating them onto substrates [6]. The

Yeongbin Lee and Seohyeon Jang contributed equally to this work.

This is an open access article under the terms of the Creative Commons Attribution-NonCommercial-NoDerivs License, which permits use and distribution in any medium, provided the original work is properly cited, the use is non-commercial and no modifications or adaptations are made.
© 2026 The Author(s). *Small* published by Wiley-VCH GmbH

inherent drawbacks of this method are i) polymeric binders such as Nafion or PTFE can partially block active sites and impede ion/electron transport [7], ii) the catalyst layers often exhibit poor adhesion and are prone to mechanical degradation during prolonged operation [8], and iii) hydrophobic binder domains impair electrolyte penetration and gas bubble release, particularly under high-current loads [9, 10]. These factors collectively lead to premature performance degradation in binder-containing electrodes under the demanding conditions (e.g., electric current density > 1 A cm^{-2}) required in practical water electrolyzers.

Binder-free architectures, in which IrO_2 nanoparticles (NPs) are directly anchored onto conductive and high-surface area supports, have therefore emerged as a compelling strategy to address the aforementioned limitations [11, 12]. Such heterogeneous catalyst-support systems enable IrO_2 NPs to disperse uniformly while suppressing NP agglomeration and substantially reducing noble-metal loading [13–15]. Furthermore, strong interfacial coupling between the IrO_2 NPs and the underlying support can modulate the electronic structure of Ir, thereby tailoring the adsorption energetics of OER intermediates and improving both activity and durability [8, 16]. In this context, the choice of support is not merely structural but plays a decisive role in governing interfacial charge redistribution, catalyst activity, and long-term operation under harsh anodic conditions.

Carbon-based supports, widely employed due to their high surface area and electrical conductivity, face intrinsic limitations under anodic OER conditions. Carbon materials are thermodynamically unstable and susceptible to electrochemical corrosion, particularly at potentials exceeding 1.4 V vs. RHE [17]. Progressive carbon oxidation not only deteriorates structural integrity but also weakens catalyst–support interactions, leading to catalyst detachment and accelerated performance decay. Moreover, the relatively inert electronic structure of carbon restricts the extent of interfacial charge redistribution with IrO_2, often limiting the catalyst–support interaction to physical anchoring rather than electronic coupling [18].

Among the various conductive support materials, Ni foam is widely recognized as an optimal platform for binder-free electrode fabrication owing to its high electrical conductivity, interconnected porous architecture, and excellent mechanical robustness [19, 20]. This unique 3D framework not only facilitates efficient charge transport and rapid gas diffusion but also offers a chemically stable and modifiable surface for heterogeneous catalyst growth. More importantly, the Ni framework provides a chemically versatile foundation that can be tuned through surface modification to form functional Ni-derived compounds, thereby allowing systematic investigation of how interfacial chemistry governs catalytic behavior [21].

Building upon this versatile Ni platform, functional Ni compounds such as nickel sulfides and phosphides have emerged as promising catalytic supports owing to their metallic conductivity, adjustable electronegativity, and diverse bonding characteristics [22]. These properties suggest the potential for stronger orbital hybridization and sustained interfacial charge transfer when coupled with noble-metal catalysts. In contrast, conventional oxide support materials (e.g., TiO_2, WO_3, and V_2O_5) are chemically stable but generally exhibit relatively low electrical conductivity and limited electronic tunability [23–25]. Although oxide supports can induce strong metal–support interactions, the extent of interfacial charge redistribution is often constrained without alloying, intentional doping, or bulk compositional modification. By comparison, nickel phosphides and sulfides can facilitate more extensive band-level hybridization with supported IrO_2, enabling more pronounced and tunable redistribution of electron density at the interface. Such support-induced electronic modulation can shift the Ir d-band center and optimize the adsorption energetics of key OER intermediates [26–29]. Despite this potential, systematic studies directly correlating support identity, interfacial electronic interactions, and catalytic performance in binder-free IrO_2 systems remain scarce. Establishing these correlations is essential for developing fundamental design principles for rational electrode engineering in practical electrolyzers.

In the present study, we developed binder-free IrO_2–Ni-based electrodes via a liquid-phase synthesis process that enabled precise control over the IrO_2 nanoparticle morphology and ultralow Ir loading (< 0.02 mg_{Ir} cm^{-2}), independent of the support material. A comparative investigation revealed that nickel phosphide (Ni_2P) was a particularly effective IrO_2-catalyst-support material, which in contrast to Ni and nickel sulfide (Ni_3S_2), enriched the electron density around Ir, accompanied by a downshift of the Ir d-band center. This electronic modulation optimized the adsorption strength of key OER intermediates (OH*, O*, and OOH*) within the adsorbate evolution mechanism pathway, resulting in markedly enhanced catalytic activity. Density functional theory (DFT) calculations further proved strong interfacial coupling between IrO_2 and Ni_2P mediated by stable interfacial bonds and Ir—O linkages, which collectively resulted in the catalyst's prolonged operational stability. This integrated Ni-based platform provides a well-defined comparative framework to elucidate how support chemistry governs the interfacial electronic structure and catalytic performance. More broadly, our findings support a generalizable strategy for interfacial support engineering in binder-free noble-metal catalysts, thereby paving the way toward cost-effective and durable electrodes for next-generation water electrolyzers.

2 | Results and Discussion

The preparation of IrO_2 deposited on Ni-based foams via liquid-phase synthesis and deposition is illustrated in Figure 1a [30]. To investigate interactions between IrO_2 and the Ni-based support materials, various types of Ni-based compounds were first fabricated by adjusting the reaction conditions and adopting specific anion sources. Using Ni foam as the starting material, Ni_3S_2 or Ni_2P were grown directly on Ni foam via sulfurization or phosphorization by utilizing di-*tert*-butyl disulfide (TBDS) or Triphenyl phosphite (TPP) as the anion source, respectively. These self-supported Ni-based compounds exhibited characteristic surface morphologies and crystal structures. Subsequently, IrO_2 NPs were deposited by immersing the support material (Ni, Ni_3S_2, or Ni_2P foam) in NaOH solution (pH 11–12) containing an Ir^{3+} precursor for 2 h at 80°C, thereby producing the analogous morphological features of the resulting IrO_2 NPs. These three types of electrode materials provided a platform to thoroughly explore the interfacial interactions between the IrO_2 and Ni-based compounds, which could influence their various properties.

16136829, 0, Downloaded from https://onlinelibrary.wiley.com/doi/10.1002/smll.74025 by Chung-Ang Library - Chung-Ang University , Wiley Online Library on [24/06/2026]. See the Terms and Conditions (https://onlinelibrary.wiley.com/terms-and-conditions) on Wiley Online Library for rules of use; OA articles are governed by the applicable Creative Commons License

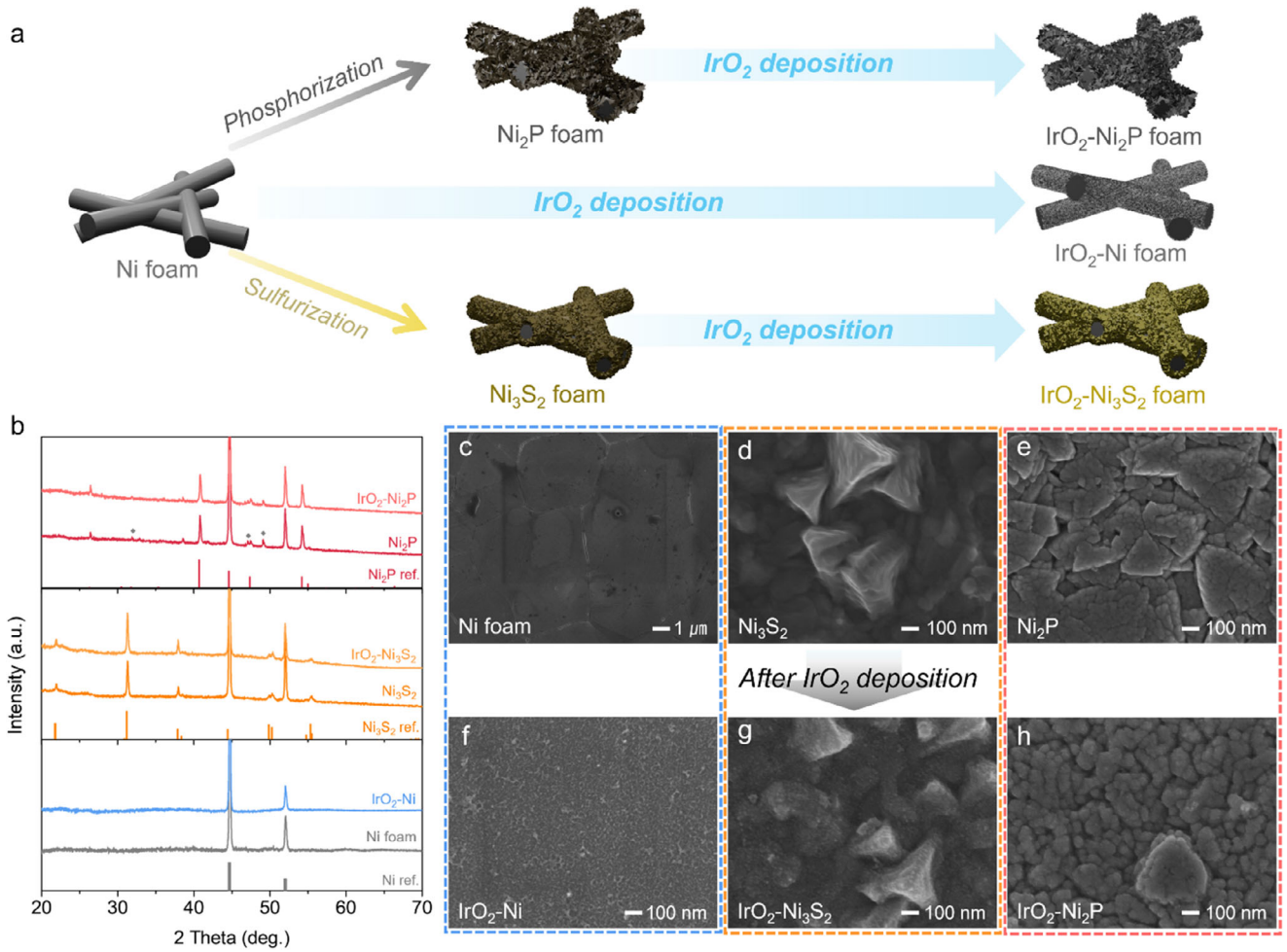


FIGURE 1 | (a) A schematic illustration of the preparation of IrO_2-deposited Ni, Ni_3S_2, and Ni_2P foams using a liquid-phase synthesis and deposition method. (b) XRD patterns for Ni foam, Ni_3S_2, Ni_2P, IrO_2-Ni, IrO_2-Ni_3S_2, and IrO_2-Ni_2P. The gray, orange, and red bars indicate Ni (PDF reference: 00-004-0850), Ni_3S_2 (PDF reference: 01-073-0698), and Ni_2P (PDF reference: 03-065-1989), respectively, while the gray diamonds indicate the $Ni_{12}P_5$ phase (PDF reference: 01-074-1381). SEM images of (c) Ni foam, (d) Ni_3S_2, (e) Ni_2P, (f) IrO_2-Ni, (g) IrO_2-Ni_3S_2, and (h) IrO_2-Ni_2P.

The X-ray diffraction (XRD) patterns in Figure 1b verify the growth of Ni-based compounds (Ni_3S_2 and Ni_2P) on Ni foam, as well as the preservation of the overall crystal structure of support materials after the IrO_2 deposition process. While pristine Ni foam exhibited only two prominent peaks at 44.5° and 51.8°, additional characteristics peaks in the patterns for the Ni_3S_2- and Ni_2P-based foams clearly indicate the formation of nickel sulfides and phosphides by aligning well with the reference peaks for heazlewoodite Ni_3S_2 and hexagonal Ni_2P, respectively, thereby confirming the self-supported growth of these compounds on Ni foam via the liquid-phase synthesis. In addition, the XRD pattern for the Ni_2P foam contained minor peaks at 32.73°, 46.96°, and 48.96°, which matched the (310), (240), and (321) planes of the $Ni_{12}P_5$ phase, respectively, signifying that nickel phosphide consisted of Ni_2P as the major phase and $Ni_{12}P_5$ as a minor phase. Moreover, after the IrO_2 deposition process, clearly identical crystal structures were maintained in all samples without the evolution of additional crystalline structure and structural transformations of Ni, Ni_3S_2, and Ni_2P. Notably, diffraction peaks indicating Ir-related species were not present in the patterns of any of the samples, which could be due to the extremely low loading amounts of Ir therein.

Ni_3S_2 and Ni_2P were successfully grown on Ni foam, with each displaying distinct surface morphological characteristics, as discernible in the scanning electron microscopy (SEM) images in Figure 1c–e. Compared to the smooth surface of pristine Ni foam (Figure 1c), that of the Ni_3S_2 foam exhibited a vertically oriented, triangular pyramid-like structure (Figure 1d) with an Ni/S atomic ratio of 60.03:39.97 (Table S1), which is consistent with the Ni_3S_2 phase. Meanwhile, the surface of the Ni_2P foam featured self-supported triangular prism structures composed of individual clusters (Figure 1e) with an Ni/P atomic ratio of 70.04:29.96 (Table S1), thus confirming the complete coverage of the Ni foam surface by the Ni-based compounds. Further structural analysis of Ni_3S_2 and Ni_2P via high-resolution transmission electron microscopy (HRTEM) revealed atomic arrangements corresponding to the (110) plane of Ni_3S_2 and the (111) plane of Ni_2P, with interplanar spacings of 2.89 and 2.21 Å, respectively (Figure S1a,b). Moreover, the scanning transmission electron microscopy-energy-dispersive X-ray spectroscopy (STEM-EDS) results confirm the uniform dispersion of elements (Figure S1c,d) and consistent atomic ratios (Table S2), thereby providing clear evidence of the formation of Ni-based compounds through the liquid-phase synthesis.

16136829, 0, Downloaded from https://onlinelibrary.wiley.com/doi/10.1002/smll.74025 by Chung-Ang Library - Chung-Ang University , Wiley Online Library on [24/06/2026]. See the Terms and Conditions (https://onlinelibrary.wiley.com/terms-and-conditions) on Wiley Online Library for rules of use; OA articles are governed by the applicable Creative Commons License

Although the unique morphologies of Ni-based foam remained largely intact after IrO_2 deposition, the surfaces became noticeably coarser, likely due to surface oxidation occurring in the NaOH solution (Figure 1f–h). Elemental analysis using SEM-EDS substantiated the presence and uniform distribution of Ir species across all samples with no significant clustering or aggregation of Ir at specific sites (Figure S2a–c). Moreover, the preserved Ni/S (61.8:37.9) and Ni/P (70.5:29.2) atomic ratios indicate that the support structures were not noticeably altered during the deposition process (Table S3).

Raman spectroscopy was employed to probe the vibrational characteristics of the catalysts and to examine possible surface oxidation and IrO_2 formation (Figure S3). All samples exhibited a broad band in the ~450–550 cm^{-1} region, which was attributed to Ni–O vibrations associated with nickel oxide/oxyhydroxide species formed via partial oxidation of the Ni-based foam [31, 32]. In addition, a weak band appearing at ~720–750 cm^{-1} corresponded to the A_{1g} phonon mode of rutile IrO_2, arising from the symmetric stretching vibration of Ir–O bonds, confirming the presence of IrO_2 on the catalyst surfaces [33].

Distinct vibrational features corresponding to the support frameworks were also observed. For IrO_2–Ni_2P, Raman bands in the ~100–200 cm^{-1} region was assigned to Ni–P lattice vibrations, while a high-wavenumber band near ~1000 cm^{-1} corresponds to P–O stretching vibrations, indicating partial oxidation of phosphorus species [34, 35]. In the case of IrO_2–Ni_3S_2, peaks in the ~200–400 cm^{-1} region were attributed to Ni–S lattice vibrations [36], together with a band near ~1000 cm^{-1} corresponding to S–O stretching vibrations, suggesting the formation of oxidized sulfur species [37]. For IrO_2–Ni, a prominent band at ~520 cm^{-1} is observed, which is attributed to Ni–O vibrations associated with surface NiOOH species, commonly formed on Ni-based electrodes. Since metallic Ni is Raman inactive, the observed Raman signals mainly originate from surface oxide/hydroxide species and the deposited IrO_2, confirming successful IrO_2 deposition and slight surface oxidation of the catalyst surface.

HRTEM imaging provides additional evidence for the successful deposition of IrO_2 onto the Ni-based form while emphasizing the consistent morphological features of the catalyst, regardless of the support type. Upon reaction with Ir^{3+} in NaOH solution, uniformly distributed ~3 nm-sized spherical nanoparticles were observed on the Ni, Ni_3S_2, and Ni_2P surfaces (Figure 2a–c, respectively). The interplanar spacing of these spherical NPs corresponded to the (200) plane of IrO_2 (a d-spacing value of ~2.25 Å [38]), thus verifying the formation of IrO_2 via the deposition method. While previous studies have reported that layered double hydroxide (LDH) structures typically incorporate Ir in its non-oxidized form, the formation of oxidized Ir on the Ni-based foams (Ni, Ni_3S_2, and Ni_2P) suggests that the reaction pathway may vary depending on the support structure [39, 40]. Furthermore, the STEM images and corresponding elemental maps demonstrate the uniform distribution of individual elements across all samples, thereby substantiating the homogeneous deposition process (Figure 2d–f). Inductively coupled plasma-mass spectrometry (ICP-MS) analysis determined the precise loading amounts of Ir species (Table S4): 0.010, 0.012, and 0.016 mg_{Ir} cm^{-2} for IrO_2-Ni, IrO_2-Ni_3S_2, and IrO_2-Ni_2P, respectively, highlighting the ultralow Ir loading in these materials. Overall, the well-controlled size and morphology of the IrO_2 NPs enabled a systematic investigation of their interaction with the Ni-based support materials, which is critical for understanding their effects on the electronic structure and, consequently, catalytic performance.

Since catalytic reactions are predominantly governed by the surface chemical states, with surface atoms directly participating in the overall reactions, the surface chemical states of the catalysts were analyzed by using X-ray photoelectron spectroscopy (XPS) to explore the electronic interactions between IrO_2 and the three types of support material (Ni, Ni_3S_2, and Ni_2P). Notably, a comparison of the Ir 4f spectra for IrO_2-Ni, IrO_2-Ni_3S_2, and IrO_2-Ni_2P in Figure 3a uncovered the influence of the Ni-based compounds on the electronic structure of Ir, as evidenced by variations in peak positions as well as the relative chemical state proportions; the primary peaks (Ir $4f_{7/2}$ and $4f_{5/2}$) appeared at the lowest binding energies in the spectrum for IrO_2-Ni_2P (62.2 and 65.2 eV, respectively), followed by IrO_2-Ni (62.48 and 65.38 eV, respectively) and IrO_2-Ni_3S_2 (62.58 and 65.58 eV, respectively), indicating differences in the oxidation state of Ir depending on the support material. These distinct shifts in the Ir oxidation states suggest that the Ni_2P support material likely donates electron density to the Ir atoms, thereby reducing their valence states. Furthermore, deconvolution of the Ir $4f_{7/2}$ and $4f_{5/2}$ peaks confirms the absence of metallic Ir, with only Ir^{3+}, Ir^{4+}, and satellite peaks typical of IrO_2 present [41, 42]. While the peak positions for Ir^{3+} (62.8 and 66 eV) and satellites (~64 and ~67 eV) did not significantly change in the spectra for the samples, the binding energies for Ir^{4+} differed depending on the support material: 62.3 and 65.3 eV for IrO_2-Ni, 62.4 and 65.45 eV for IrO_2-Ni_3S_2, and 62.1 and 65.1 eV for IrO_2-Ni_2P. These shifts further corroborate the finding that Ir in IrO_2-Ni_2P attained the lowest oxidation state. Since prior studies have shown that a higher proportion of the lower-valence state (3^+) is favorable for catalyzing the OER [43, 44], the ratios for the Ir^{3+} and Ir^{4+} states were calculated to quantify these observations (Table S5). Among the samples, IrO_2-Ni_2P had the highest Ir^{3+}/Ir^{4+} ratio (0.61), followed by IrO_2-Ni (0.41) and IrO_2-Ni_3S_2 (0.31). These opposing shifts provide direct evidence of strong electron donation from the Ni_2P support to IrO_2. As will be further elucidated by DFT calculations, this electron-rich environment at the Ir active sites downshifts the Ir d-band center, thereby optimizing the adsorption strength of OER intermediates [45–47]. Furthermore, the lower oxidation state of Ir in IrO_2-Ni_2P is expected to enhance catalytic efficiency and durability under the harsh conditions of the OER by mitigating Ir over-oxidation and subsequent dissolution [48].

The Ni 2p spectra for the samples in Figure 3b contain prominent peaks corresponding to Ni^{2+}, Ni^{3+}, and their satellites, along with characteristic peaks indicative of the chemical states for Ni metal (852.6 eV), nickel sulfide (853 eV), or nickel phosphide (853.5 eV) species. In the Ni 2p spectra for Ni_3S_2 and Ni_2P, two pairs of intense peaks appeared in the higher binding energy region compared to Ni metal (Ni^0; 852.6 eV) [49], which is attributable to Ni-S bonds (853.05 and 870.35 eV for Ni_3S_2 [50]) and Ni—P bonds (853.5 and 870.73 eV for Ni_2P [28]) (Figure S4a). Additional peaks corresponding to Ni^{2+} (855.9 and 873.66 eV for Ni_3S_2; 856.05 and 873.52 eV for Ni_2P) and satellites (861.25 and 880.02 eV for Ni_3S_2; 860.91 and 878.6 eV for Ni_2P) were also

16136829, 0, Downloaded from https://onlinelibrary.wiley.com/doi/10.1002/smll.74025 by Chung-Ang Library - Chung-Ang University , Wiley Online Library on [24/06/2026]. See the Terms and Conditions (https://onlinelibrary.wiley.com/terms-and-conditions) on Wiley Online Library for rules of use; OA articles are governed by the applicable Creative Commons License

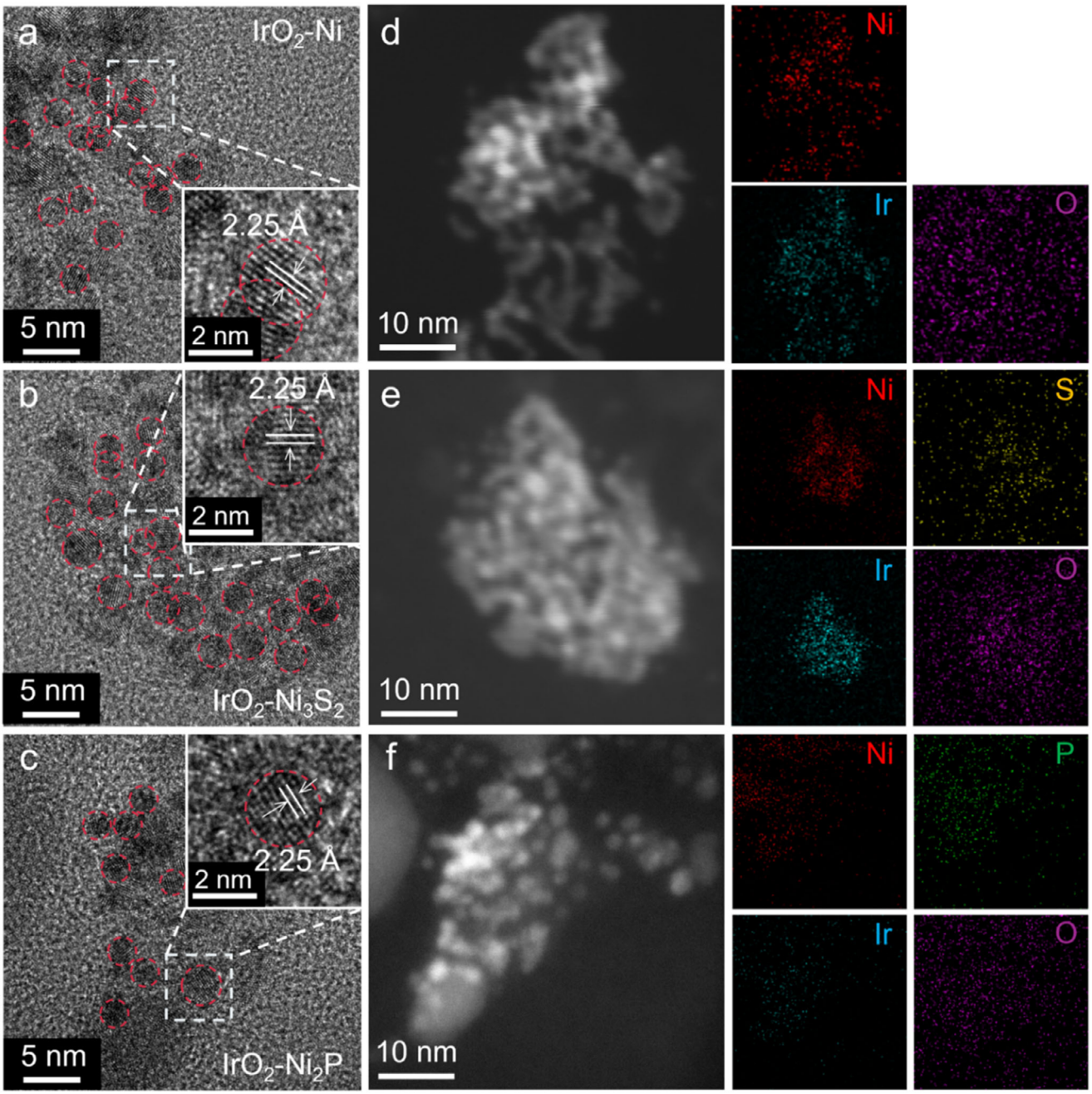


FIGURE 2 | TEM images of (a) IrO_2-Ni, (b) IrO_2-Ni_3S_2, and (c) IrO_2-Ni_2P. The red circles indicate IrO_2 NPs. Inset: an HRTEM image of the IrO_2 NPs. STEM images with corresponding elemental maps for (d) IrO_2-Ni, (e) IrO_2-Ni_3S_2, and (f) IrO_2-Ni_2P.

present. Notably, in the spectra for IrO_2-Ni, IrO_2-Ni_3S_2, and IrO_2-Ni_2P, the emergence of Ni^{3+} peaks (857.5 and 874.9 eV for IrO_2-Ni; 857.5 and 874.8 eV for IrO_2-Ni_3S_2; and 857.9 and 875.3 eV for IrO_2-Ni_2P) likely originated from NiOOH species formed via surface oxidation during IrO_2 deposition in NaOH solution. In addition to the Ni^{3+} state, peaks corresponding to Ni^{2+} were observed at a higher binding energy in IrO_2-Ni_2P (856 and 873.5 eV) compared to IrO_2-Ni (855.8 and 873.3 eV) and IrO_2-Ni_3S_2 (855.8 and 873.2 eV), thereby indicating a reversed trend relative to the Ir 4f spectra. The O 1s spectra for all of the samples reveal the presence of four distinct oxygen species: lattice O (530.5 eV), Ir—OH (~531.15 eV), Ni—OH (~531.9 eV), and adsorbed H_2O (~532.9 eV) (Figure 3c) [51, 52]. In addition, after IrO_2 deposition, the S 2p and P 2p spectra in Figures S4b,c, and S5 are characteristic of typical nickel sulfides [26]. and phosphides [53], respectively, confirming the structural integrity of the support materials. Despite the similar morphology of IrO_2 NPs across the different support materials, the electronic structures of Ir and Ni were significantly affected by the type of support, thus indicating that IrO_2-support interactions are likely to affect catalytic properties.

The OER activity of IrO_2 deposited on Ni-based supports, along with the bare supports and commercial IrO_2 on carbon paper (CP) (IrO_2/CP) reference, was evaluated in 1 M KOH electrolyte using a three-electrode system. To minimize interference from non-OER currents arising from the Ni oxidation of the Ni foam

16136829, 0, Downloaded from https://onlinelibrary.wiley.com/doi/10.1002/smll.74025 by Chung-Ang Library - Chung-Ang University , Wiley Online Library on [24/06/2026]. See the Terms and Conditions (https://onlinelibrary.wiley.com/terms-and-conditions) on Wiley Online Library for rules of use; OA articles are governed by the applicable Creative Commons License

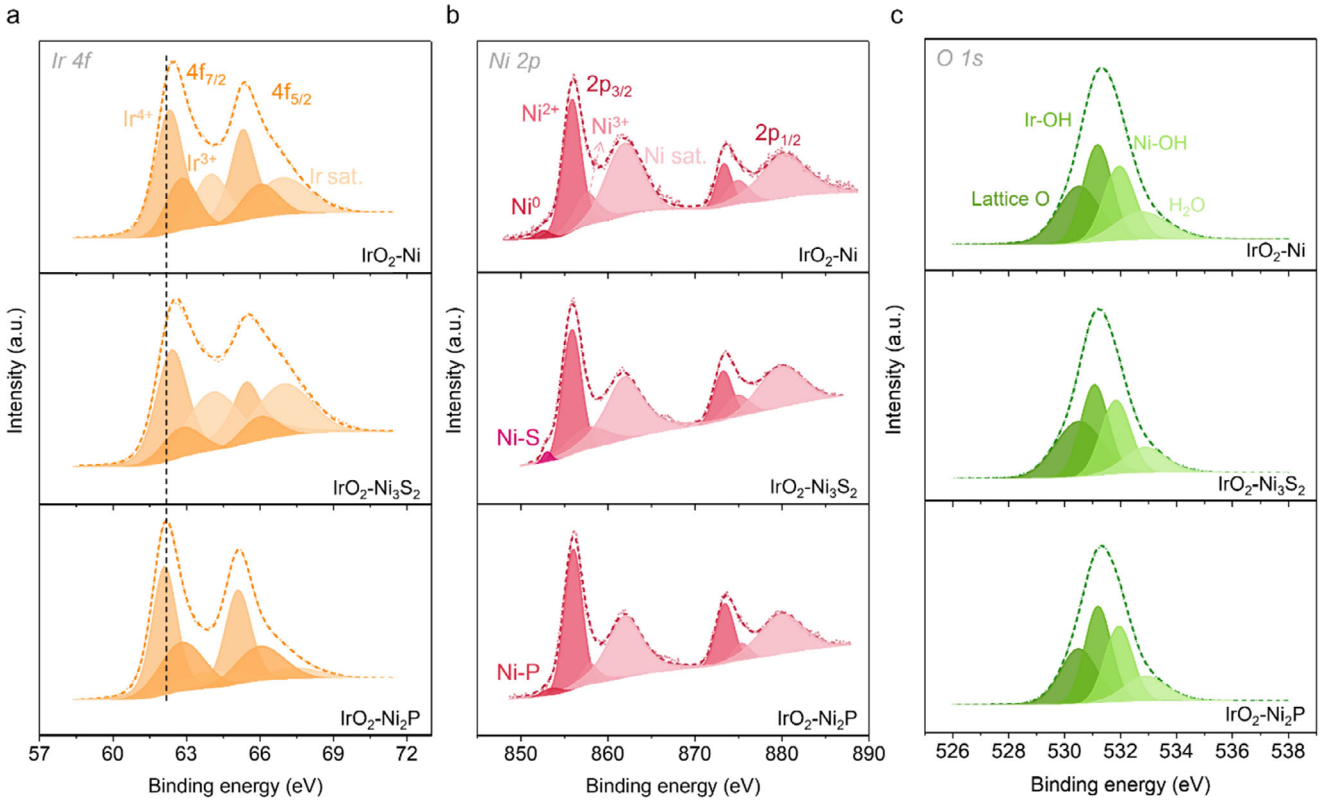


FIGURE 3 | XPS (a) Ir 4f, (b) Ni 2p, and (c) O 1s spectra for IrO_2-Ni, IrO_2-Ni_3S_2, and IrO_2-Ni_2P.

substrate, all OER polarization curves were extracted from the reverse scan to enable accurate comparison among the catalysts [54]. As shown in Figure 4a, IrO_2-Ni_2P demonstrated remarkably higher OER performance than the other samples across the entire current density range. Specifically, IrO_2-Ni_2P achieved the lowest overpotentials of 232 and 309 mV at current densities of 10 and 100 mA cm^{-2}, respectively, thus reflecting the optimized surface Ir chemical states, which are highly favorable for catalyzing the OER. Furthermore, the higher activity of IrO_2-Ni (287 mV at 10 mA cm^{-2}) compared to IrO_2-Ni_3S_2 (306 mV at 10 mA cm^{-2}) highlights the strong correlation between surface chemical states and catalytic activity. Although the commercial IrO_2/CP reference (305 mV at 10 mA cm^{-2}) displayed slightly higher activity than IrO_2-Ni_3S_2 at a low current density, this trend was reversed at higher current density, highlighting the superior IrO_2–support interactions of our catalyst compared to the conventional counterpart in high-current regions. Among the support materials, Ni_2P exhibited the highest activity (365 mV at 10 mA cm^{-2}), which emphasizes the importance of engineering highly active support materials (408 mV at 10 mA cm^{-2} for Ni_3S_2 and 435 mV at 10 mA cm^{-2} for Ni) (Figure S6). Thus, the interaction between IrO_2 and Ni_2P led to exceptional OER performance, thus highlighting the critical role of the chemical states therein in determining the catalytic properties.

To provide insights into the reaction kinetics and charge-transfer behavior resulting in the distinguished catalytic properties of IrO_2-Ni_2P, Tafel and electrochemical impedance spectroscopy (EIS) analyses were further conducted (Figure 4b,c). Although the complex OER mechanism limits the direct elucidation of the reaction pathway from a Tafel slope alone, the remarkably low Tafel slope (71.6 mV dec^{-1}) and charge-transfer resistance (R_{ct} = 4.86 Ω) of IrO_2-Ni_2P ascertained its rapid reaction kinetics and efficient charge transfer, both of which are closely correlated with its exceptional catalytic efficiency. Furthermore, the observed trends in Tafel slopes (77.1 mV dec^{-1} for IrO_2-Ni, 79.4 mV dec^{-1} for IrO_2/CP, and 86.7 mV dec^{-1} for IrO_2-Ni_3S_2) and R_{ct} values (5.53 Ω for IrO_2-Ni, 5.92 Ω for IrO_2/CP and 6.44 Ω for IrO_2-Ni_3S_2) are consistent with the OER activity since a lower Tafel slope and charge-transfer resistance are indicative of enhanced electrocatalytic performance. To gain a deeper understanding of the charge-transfer kinetics during the OER, in situ EIS was conducted under various applied potentials (1.20—1.55 V) (Figure 4d and Figure S7) [55]. The Bode phase plots in Figure 4e indicate that IrO_2-Ni_2P featured a more rapid abatement of the phase angle in the low frequency region with an increase in applied potential compared to IrO_2-Ni and IrO_2-Ni_3S_2. Such behavior highlights the crucial role of the support material in improving the electrocatalytic kinetics and directly influencing the OER activity [56].

Given the varying influence of surface morphology on OER performance depending on the electrodes, the intrinsic catalytic activity therein was evaluated to focus on the inherent catalytic properties of the materials. Cyclic voltammetry (CV) curves were obtained over an identical potential range at different scan rates, exhibiting capacitor-like behavior in the electrocatalysts (Figure S8). The linear relationship between current density and scan rate was used to determine the surface area of each catalyst (quantified by using the slope), which corresponds to the electrochemical double-layer capacitance (C_{dl}) (Figure 4f). The significantly larger C_{dl} value for IrO_2-Ni_2P (6.80 mF cm^{-2}) indicates the presence

16136829, 0, Downloaded from https://onlinelibrary.wiley.com/doi/10.1002/smll.74025 by Chung-Ang Library - Chung-Ang University , Wiley Online Library on [24/06/2026]. See the Terms and Conditions (https://onlinelibrary.wiley.com/terms-and-conditions) on Wiley Online Library for rules of use; OA articles are governed by the applicable Creative Commons License

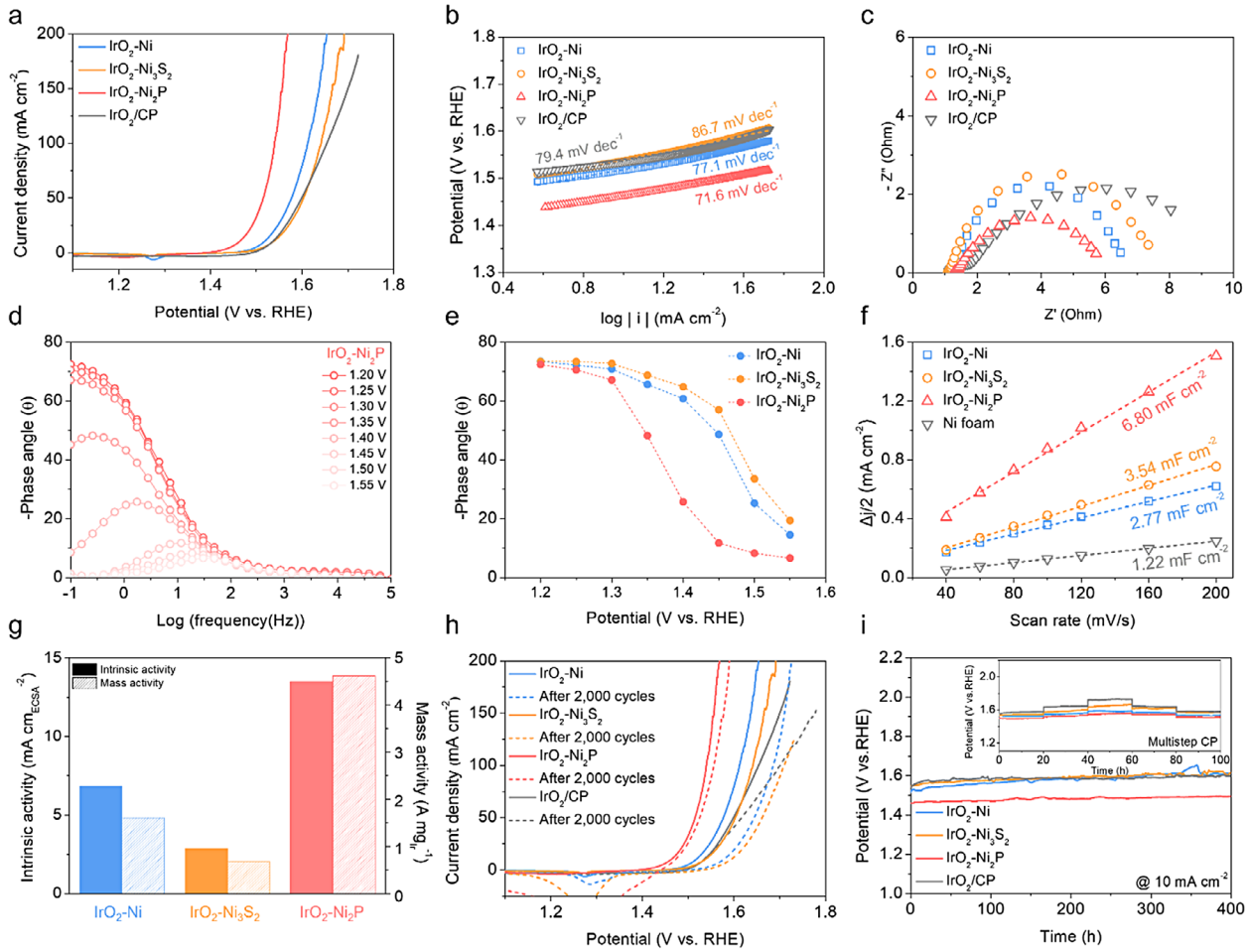


FIGURE 4 | Alkaline OER performance of the as-prepared electrodes in 1 M KOH. (a) Polarization curves. (b) Tafel plots for IrO_2-Ni, IrO_2-Ni_3S_2, IrO_2-Ni_2P, and IrO_2/CP derived from the OER polarization curves. (c) Nyquist plots at an applied overpotential of 0.58 V (vs. Hg/HgO). (d) Bode phase plots of IrO_2-Ni_2P. (e) Phase peak angle responses of IrO_2-Ni, IrO_2-Ni_3S_2, and IrO_2-Ni_2P at various applied potentials. (f) Electrochemical double-layer capacitances of IrO_2-Ni, IrO_2-Ni_3S_2, IrO_2-Ni_2P, and Ni foam. (g) A histogram of specific activity and mass activity at an overpotential of 300 mV. (h) Polarization curves for IrO_2-Ni, IrO_2-Ni_3S_2, IrO_2-Ni_2P, and IrO_2/CP before and after ADT over 2000 cycles. (i) Chronopotentiometry curves for IrO_2-Ni, IrO_2-Ni_3S_2, IrO_2-Ni_2P, and IrO_2/CP at 10 mA cm^{-2}. Inset: Multi-step chronopotentiometry curves after sequentially applying current densities of 20, 50, 100, 50, and 20 mA cm^{-2}.

of abundant active areas that contribute to its superior catalytic activity. In addition, the IrO_2-deposited samples exhibited higher C_{dl} values compared to Ni foam (1.22 mF cm^{-2}), with IrO_2-Ni_3S_2 (3.54 mF cm^{-2}) having a slightly larger value than IrO_2-Ni (2.77 mF cm^{-2}), likely due to the morphological effects of the support materials. The intrinsic activity was subsequently compared based on C_{dl}, which exhibited a proportional relationship with the electrochemically active surface area (ECSA); the latter was estimated by dividing C_{dl} by the specific capacitance (C_s) of a flat surface electrode, for which we took the measured value of 1.22 mF cm^{-2} for Ni foam. Notably, the ECSA-normalized polarization curves confirm that IrO_2-Ni_2P exhibited the highest intrinsic current density at an overpotential of 300 mV (13.5 mA cm_{ECSA}^{-2}), followed by IrO_2-Ni (6.85 mA cm_{ECSA}^{-2}) and IrO_2-Ni_3S_2 (2.85 mA cm_{ECSA}^{-2}), thereby highlighting the distinguished catalytic efficiency of the active sites in IrO_2-Ni_2P (Figure 4g and Figure S9a). Furthermore, IrO_2-Ni_2P featured an outstanding mass activity of 4.6 A mg^{-1} at 1.53 V, far surpassing that of previously reported noble-metal-based OER catalysts (Figure 4g and Figure S9b, and Table S6). This exceptional mass activity, achieved with extremely low Ir loading, highlights the efficient utilization of Ir atoms (an essential factor in noble-metal-based electrocatalysts). Moreover, the remarkable inherent catalytic activity of IrO_2-Ni_2P placed an emphasis on modulating the surface chemical states arising from the synergistic interactions between IrO_2 and Ni_2P.

The beneficial effects of IrO_2–support interfacial interactions were further corroborated by comparing the catalytic activity of chemically deposited IrO_2-Ni_2P with that of physically attached commercial IrO_2 on Ni_2P foam (Com. IrO_2-Ni_2P). While ensuring the same Ir-loading amount (0.016 mg cm^{-2}), the Com. IrO_2-Ni_2P electrode was fabricated by simply drop-casting a commercial IrO_2-containing solution onto Ni_2P foam, signifying a system with only physical interactions between the components. A comparison of OER activity revealed that the interfacial interactions between IrO_2 and Ni_2P significantly improved catalytic performance, with IrO_2-Ni_2P exhibiting superior OER performance compared to Com. IrO_2-Ni_2P (Figure S10). The active surface area and inherent activity were also investigated while

16136829, 0, Downloaded from https://onlinelibrary.wiley.com/doi/10.1002/smll.74025 by Chung-Ang Library - Chung-Ang University , Wiley Online Library on [24/06/2026]. See the Terms and Conditions (https://onlinelibrary.wiley.com/terms-and-conditions) on Wiley Online Library for rules of use; OA articles are governed by the applicable Creative Commons License

considering differences in the size and morphology of commercial IrO_2 and chemically deposited IrO_2 NPs (Figure S11). The C_{dl} value for IrO_2-Ni_2P (6.80 mF cm^{-2}) was approximately twice that for Com. IrO_2-Ni_2P (3.39 mF cm^{-2}), while the intrinsic activity of the former (13.5 mA $cm_{ECSA}{}^{-2}$ at 1.53 V) was nearly four times higher than that of the latter (3.30 mA $cm_{ECSA}{}^{-2}$ at 1.53 V) (Figure S12). The increments in intrinsic activity and the enlarged active surface area seen in IrO_2-Ni_2P are attributed to the chemical deposition process, which not only created favorable chemical states for catalytic reactions but also facilitated strong mutual interactions between IrO_2 and Ni_2P, thereby significantly enhancing the catalytic properties (Figure S13).

In addition to the remarkable activity, various stability tests under harsh conditions verified the catalytic robustness of IrO_2-Ni_2P. During the accelerated degradation test (ADT), IrO_2-Ni_2P exhibited the smallest deviation in OER polarization curves before and after 2,000 CV cycles at a scan rate of 100 mV s^{-1}, with only a 10 mV increase in overpotential at 10 mA cm^{-2} (Figure 4e). In contrast, IrO_2-Ni and IrO_2-Ni_3S_2 showed significant attenuation, with an overpotential increase of approximately 60 mV, exhibiting their vulnerability to a rapidly fluctuating voltage. Although the performance of IrO_2/CP at 10 mA cm^{-2} remained nearly unchanged, the polarization curve exhibited a shift toward lower activity, thereby suggesting a significant deterioration in the reaction kinetics therein. As well as stable operation during multi-step chronopotentiometry test, IrO_2-Ni_2P sustained ~90% of its initial catalytic performance after 400 h of testing at 10 mA cm^{-2}, while the others were lower (~66% for IrO_2-Ni, ~77% for IrO_2-Ni_3S_2, and ~82% IrO_2-CP), thereby confirming the exceptional durability of IrO_2-Ni_2P (Figure 4f).

After OER analysis figured out the structural inertness and changes in surface chemical states of the samples, as well as uncovering the underlying factors contributing to the superior electrocatalytic performance of IrO_2-Ni_2P. While the surfaces of IrO_2-Ni, IrO_2-Ni_3S_2, and IrO_2-Ni_2P appeared to have undergone inevitable oxidation during OER, the SEM images confirm that their morphological characteristics were well preserved (Figure S14a–f). In addition, there were no noticeable variations in XRD patterns before and after OER test (Figure S15), which highlights the structural robustness of the electrodes crucial for ensuring long-term operability. The long-lasting catalytic behavior of IrO_2-Ni_2P could be linked to the low oxidation state of Ir, as demonstrated via XPS (Figure S16a). During the OER process, the surface chemical states underwent inevitable modulation due to the gradual oxidation of metal species [38]. Despite an overall increase in the oxidation state of Ir, the primary peaks (Ir $4f_{7/2}$ and $4f_{5/2}$) were located at lower binding energies in the XPS profile for IrO_2-Ni_2P (62.3 and 65.3 eV) than seen in those for IrO_2-Ni (62.6 and 65.6 eV) and IrO_2-Ni_3S_2 (62.7 and 65.7 eV). This relatively low oxidation state of Ir in IrO_2-Ni_2P contributed to the retention of its catalytic properties during the OER by effectively mitigating over-oxidation that could otherwise cause Ir dissolution and a subsequent decline in activity. Meanwhile, the binding energies of each chemical state in the Ni 2p spectra for the samples after the OER remained nearly unchanged, although an increase in signal in the Ni 3p region was observed in the Ir 4f spectra (Figure S16b). In addition, although the O 1s spectra for the samples consistently revealed four distinct oxygen species (lattice O, Ir-OH, Ni-OH, and adsorbed H_2O) at similar binding energies before and after the OER, the relative peak areas varied (Figure S16c). The proportion of lattice oxygen was well preserved in IrO_2-Ni_2P, whereas it decreased in IrO_2-Ni and IrO_2-Ni_3S_2, implying enhanced stability of IrO_2-Ni_2P, due to the robustness of its surface oxygen species (Figure S17) [4]. Our findings suggest that Ni_2P is an ideal support material for interacting with IrO_2, thereby optimizing the chemical states that facilitate the OER and long-term operation.

DFT calculations were performed to elucidate the intrinsic influence of the Ni-based supports on the OER performance of IrO_2. Prior to the calculations, electrochemical analysis using tetramethylammonium hydroxide (TMAOH) as the electrolyte was conducted to distinguish between the adsorption evolution mechanism (AEM) and the lattice oxygen oxidation mechanism (LOM). It has been well established that TMA^+ can selectively interact with surface $O_2{}^{2-}/O^-$-like intermediates, which are characteristic signatures of the LOM pathway. Such interactions are known to suppress OER kinetics when TMAOH is introduced into the electrolyte, due to the stabilization or blocking of lattice oxygen–related reactive species [57, 58]. However, the polarization curves measured in 1 M TMAOH exhibited no significant current decrease compared to those in the KOH environment, suggesting that the LOM pathway is not activated (Figure S18). Furthermore, to thermodynamically analyze the experimental observations derived from the TMAOH electrolyte system, we performed DFT calculations to evaluate the free energy profiles of both the AEM and the LOM on IrO_2-Ni, IrO_2-Ni_3S_2, and IrO_2-Ni_2P surfaces (Figure S19) [59]. The calculated OER overpotentials (η_{OER}) are consistently lower for the AEM than for the LOM across all samples. This indicates that the oxygen intermediates bind very strongly to the catalyst surface, making the formation of oxygen vacancies (V_O) thermodynamically uphill [60]. Consequently, the generation of LOM-specific reactive intermediates (e.g., $O_2{}^{2-}/O^-$) is significantly suppressed, which prevents interaction with TMA^+. These experimental observations strongly suggest that the OER in this catalyst system predominantly follows the AEM pathway. Accordingly, subsequent DFT calculations were performed based on the AEM.

Given the ultralow loading amount of IrO_2 in the experimental system, the computational model adopted a rutile IrO_2 (110) cluster as an island supported on Ni (111), Ni_2P (001), and Ni_3S_2 (0001) substrates (Figure S20). The on-top sites of the Ir atoms in IrO_2-Ni, IrO_2-Ni_3S_2, and IrO_2-Ni_2P served as the active centers for binding OER intermediates *O, *OH, and *OOH (Figure 5a–c). The computed free-energy profiles of the OER steps at U = 0 and 1.23 V for IrO_2-Ni, IrO_2-Ni_3S_2, and IrO_2-Ni_2P in Figure 5d reveal that the rate-determining step (RDS) corresponds to the formation of the Ir-OOH* intermediate from Ir—O* across all of the calculated configurations, which is consistent with the conventional adsorbate evolution mechanism of IrO_2. Importantly, the IrO_2-Ni_2P system exhibited the lowest free-energy barrier of 2.2 eV, underscoring its thermodynamically favorable pathway for the OER. By contrast, IrO_2–Ni_3S_2 and IrO_2–Ni both showed higher free-energy barriers of 2.5 eV, which is in agreement with the experimental observations. As summarized in Table S7, IrO_2-Ni_2P also showed the weakest oxygen adsorption energy (E_{O^*} = 2.0 eV compared to 1.7 and 1.8 eV for IrO_2-Ni and IrO_2-Ni_3S_2, respectively). Since excessively strong O adsorption can hinder O—O coupling and limit the overall reaction rate,

16136829, 0, Downloaded from https://onlinelibrary.wiley.com/doi/10.1002/smll.74025 by Chung-Ang Library - Chung-Ang University , Wiley Online Library on [24/06/2026]. See the Terms and Conditions (https://onlinelibrary.wiley.com/terms-and-conditions) on Wiley Online Library for rules of use; OA articles are governed by the applicable Creative Commons License

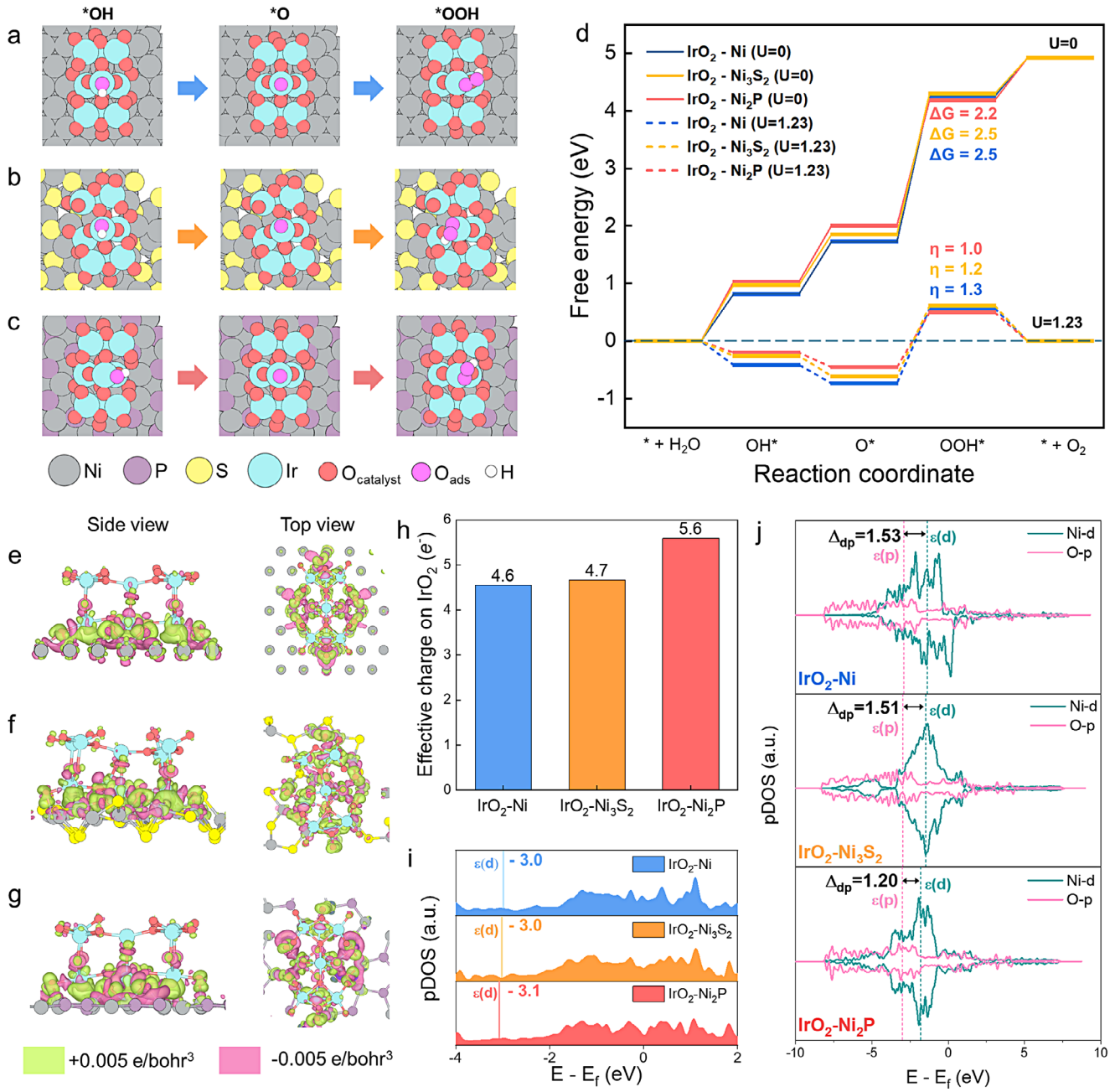


FIGURE 5 | The optimized structures of (a) IrO_2-Ni, (b) IrO_2-Ni_3S_2, and (c) IrO_2-Ni_2P interacting with OER intermediates OH*, O*, and OOH*. (d) An energy diagram for the OER process on IrO_2-Ni, IrO_2-Ni_3S_2, and IrO_2-Ni_2P at 0 V and 1.23 V. Side and top views of charge density differences in the interfaces with (e) IrO_2-Ni, (f) IrO_2-Ni_3S_2, and (g) IrO_2-Ni_2P (the green and pink regions reflect electron-rich and electron-deficient areas, respectively). (h) Accumulated electron density in IrO_2 on each surface. (i) Calculated partial density of state (pDOS) of Ir d-band in the IrO_2-Ni, IrO_2-Ni_3S_2, and IrO_2-Ni_2P surfaces. The Arabic numbers indicate the Ir d-band center in each surface. (j) Calculated pDOS of Ni d-band and O p-band in the IrO_2-Ni, IrO_2-Ni_3S_2, and IrO_2-Ni_2P surfaces. The green and pink dashed lines indicate the d-band and p-band centers, respectively. The Arabic numbers denote the gaps (Δ_{dp}) between the d-band and p-band centers.

the moderate weakening of M—O* binding observed in IrO_2-Ni_2P effectively lowers the barrier for M—OOH* formation and thereby enhances the OER kinetics [61].

Further investigations into the interfacial electronic interactions provided critical insights into the exceptional catalytic behavior of IrO_2 supported on Ni_2P. Unlike the other supports, IrO_2-Ni_2P forms distinct bonding interactions between the oxygen atoms in IrO_2 and both the phosphorus and nickel atoms in the Ni_2P support (Figure S21). Bader charge analysis revealed that IrO_2-Ni_2P accumulates a greater electron density on the IrO_2 surface (5.6) compared with those in IrO_2-Ni and IrO_2-Ni_3S_2 (4.6 and 4.7 electrons, respectively) (Figure 5e–h). This result indicates more efficient electron transfer from the Ni_2P support to IrO_2 than from Ni or Ni_3S_2, thereby enriching the electron density of Ir sites and modulating their electronic structures. This theoretical finding perfectly aligns with our earlier XPS observations (Figure 3). Specifically, the opposing shifts of the Ir $4f_{7/2}$ peak to the lowest

16136829, 0, Downloaded from https://onlinelibrary.wiley.com/doi/10.1002/smll.74025 by Chung-Ang Library - Chung-Ang University , Wiley Online Library on [24/06/2026]. See the Terms and Conditions (https://onlinelibrary.wiley.com/terms-and-conditions) on Wiley Online Library for rules of use; OA articles are governed by the applicable Creative Commons License

binding energy (62.2 eV) and the Ni $2p_{3/2}$ peak to the highest binding energy (856 eV) provide direct experimental evidence of this electron donation. Consequently, the highest Ir^{3+}/Ir^{4+} ratio (0.61) observed in IrO_2-Ni_2P corroborates the establishment of an electron-rich environment at the Ir active sites. Such electron enrichment was also reflected in the position of the Ir d-band center downshifting to −3.1 eV in IrO_2-Ni_2P compared with −3.0 eV in IrO_2-Ni and IrO_2-Ni_3S_2 (Figure 5i). A lower d-band center corresponds to a higher occupancy of antibonding states, which weakens the binding strength between IrO_2 and the oxygenated intermediates. Accordingly, this moderation of adsorption energetics facilitates oxygen release and accelerates the overall OER process [25].

The electronic alignment and interfacial bonding stability at the IrO_2-support interfaces were evaluated by calculating the energy difference (ΔE_dp) between the Ni d-band center in supports and the O p-band center in IrO_2 (Figure 5j). The IrO_2-Ni_2P interface featured the smallest ΔE_dp of 1.20 eV (1.53 and 1.51 eV for the IrO_2-Ni and IrO_2-Ni_3S_2 interfaces, respectively), which is indicative of the best orbital alignment and most stable interfacial bonding. This result was further corroborated by the calculated Ir–O bond length variation relative to pure IrO_2, which followed the order IrO_2-Ni_2P (102.0%) < IrO_2-Ni (102.8%) < IrO_2-Ni_3S_2 (105.6%) (Table S8). The minimal lattice distortion observed in IrO_2-Ni_2P is expected to enhance the structural compatibility and greater preservation of Ir–O bond integrity within the IrO_2 lattice. These favorable structural and orbital characteristics fundamentally explain why Ni_2P acts as the most highly efficient electron donor among the supports. This optimized interface facilitates a more effective pathway for electron transfer, thereby enriching the electron density on the IrO_2 surface and inducing a downward shift of the Ir d-band center. This electronic reconfiguration allows the O intermediate to achieve an optimal adsorption strength, being neither too strong nor too weak. Ultimately, from the fundamental interfacial orbital alignment to the minimized RDS free energy barrier, underpins its superior catalytic activity and durability during the OER.

Building on the theoretical predictions, the applicability of IrO_2-Ni_2P was evaluated as a practical anode in an anion exchange membrane water electrolyzer (AEMWE) system. Guided by the half-cell OER results and DFT insights, the IrO_2-Ni_2P sample was integrated as the anode catalyst in an AEMWE system, and its performance and durability were benchmarked against a commercial IrO_2/CP electrode (Figure 6a). The AEMWE single-cell polarization curves were obtained for two different membrane electrode assembly (MEA) configurations over a potential range of 1.0–2.0 V_{cell}, flowing 1.0 M KOH (preheated to 80°C) as the electrolyte. Remarkably, the IrO_2-Ni_2P || Pt/C/CP configuration achieved a current density of 3.1 A cm^{-2} @ 2.0 V_{cell}, whereas the IrO_2/CP || Pt/C/CP configuration reached only 1.9 A cm^{-2} under identical conditions (Figure 6b). The performance gap was particularly pronounced at current densities exceeding 1 A cm^{-2}, which was attributed to the enhanced mass transport in the self-supported IrO_2-Ni_2P electrode not requiring a polymeric binder. The AEMWE single-cell test results clearly demonstrate the advantages of the binder-free IrO_2-Ni_2P architecture, particularly in achieving high activity at large current densities, which is particularly challenging for conventional powder-based electrodes. Moreover, the IrO_2/CP || Pt/C/CP exhibited superior single-cell performance compared with previously reported noble-metal-based AEMWE systems (Table S9).

To further elucidate the mass-transport characteristics, contact angle measurements were conducted to assess electrode surface hydrophilicity. Although IrO_2 is inherently hydrophilic, the incorporation of polytetrafluoroethylene (PTFE) binder (commonly used in conventional electrode fabrication) significantly reduced such property, resulting in a hydrophobic surface with a large contact angle exceeding 100° (Figure 6c and Figure S22) [62]. In contrast, the binder-free electrodes (IrO_2-Ni, IrO_2-Ni_3S_2, and IrO_2-Ni_2P) preserved the intrinsic hydrophilicity of IrO_2 by eliminating binder-induced surface modifications, resulting in markedly lower contact angles, with the IrO_2-Ni_2P electrode displaying the lowest one (21.4°) (Figure 6c and Table S10). This highlights the crucial role of both support selection and a binder-free fabrication strategy to simultaneously optimize the physicochemical and catalytic properties.

To better understand the performance characteristics of each AEMWE single cell, the overall cell overpotential was subdivided into three distinct components: ohmic overpotential (η_{ohm}), kinetic overpotential (η_{kin}), and mass-transfer overpotential (η_{mass}) (Figure 6d,e). Ohmic resistance (R_{ohm}) values were extracted from Nyquist plots and used to calculate η_{ohm} according to the relationship $\eta_{ohm} = iR_{ohm}$ (Figure S23). η_{kin} values were determined from Tafel plots of iR_{ohm}-corrected I-V curves (Figure S24). Subsequently, η_{mass} values were calculated by subtracting other components from the total cell voltage via the equation $\eta_{mass} = E_{cell} - E_{rev} - \eta_{ohm} - \eta_{kin}$. A notable difference between the two AEMWE systems was identified in the ohmic and mass-transport overpotential regions, which contributed to the enhanced performance of the AEMWE system employing the IrO_2-Ni_2P anode. The IrO_2-Ni_2P electrode showed a significantly lower ohmic resistance (R_{ohm}) (0.05 Ω cm^2) in the AEMWE system than that observed with the spray-coated IrO_2/CP anode (0.11 Ω cm^2), resulting in a smaller ohmic overpotential over the entire current density range (Figure S25). In addition, the AEMWE with the IrO_2-Ni_2P anode exhibited a lower η_{mass} at high-current densities, which could have originated from the hydrophilic nature of the binder-free system facilitating rapid KOH transport to the catalytic sites and detachment of oxygen bubbles [63]. Although the IrO_2-Ni_2P || Pt/C/CP configuration showed a somewhat higher η_{kin} than IrO_2/CP || Pt/C/CP, presumably due to the considerably higher Ir loading in the latter (3.0 mg cm^{-2}), the substantial reduction in ohmic and mass-transport overpotentials in the IrO_2-Ni_2P anode enabled the AEMWE system to deliver a markedly higher overall performance, particularly at current densities >1 A cm^{-2} (Figure S26). Long-term durability test further underscored this advantage. At 1 A cm^{-2}, the IrO_2/CP || Pt/C/CP system suffered severe performance degradation (34.1 mV h^{-1}), potentially due to mechanical stress on the catalyst layers and subsequent delamination under vigorous gas evolution [64]. On the contrary, the IrO_2-Ni_2P-based AEMWE maintained stable operation with a much lower decay rate of 7.84 mV h^{-1}, reflecting the mechanical robustness of the binder-free IrO_2-Ni_2P electrode. Taken together, these results highlight the remarkable activity and durability of IrO_2-Ni_2P in both half-cell and single-cell configurations. The findings confirm that the rational support design combined with binder-free catalyst growth offers an effective pathway to overcome the intrinsic limitations of

16136829, 0, Downloaded from https://onlinelibrary.wiley.com/doi/10.1002/smll.74025 by Chung-Ang Library - Chung-Ang University , Wiley Online Library on [24/06/2026]. See the Terms and Conditions (https://onlinelibrary.wiley.com/terms-and-conditions) on Wiley Online Library for rules of use; OA articles are governed by the applicable Creative Commons License

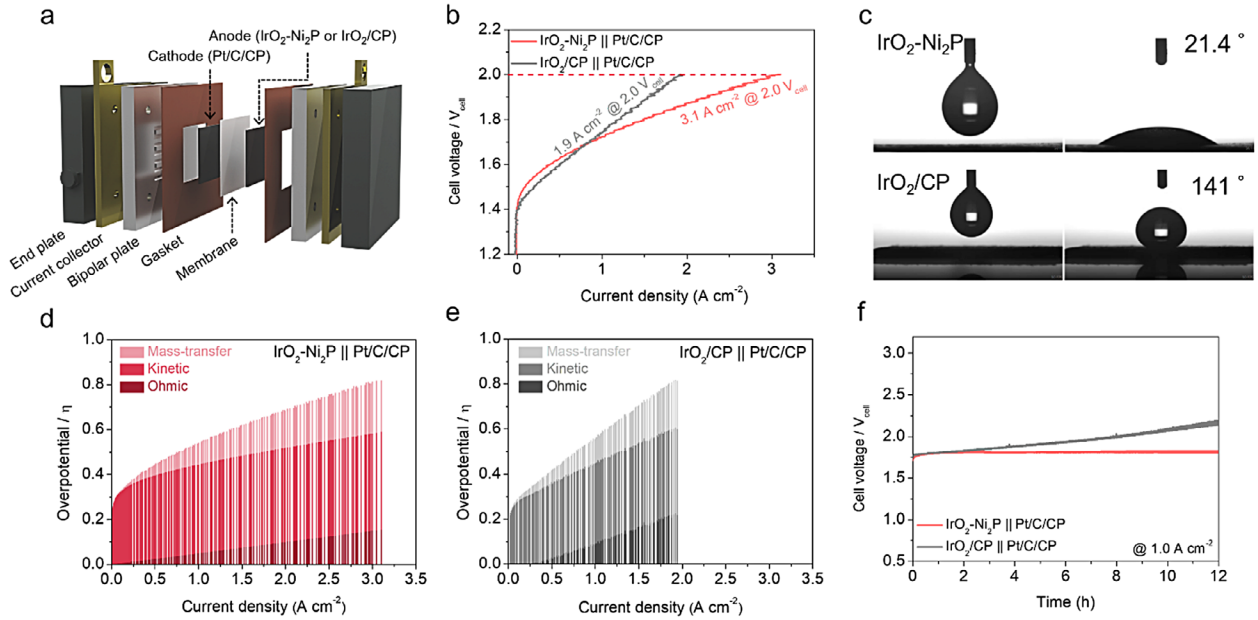


FIGURE 6 | AEMWE single-cell performance. (a) A schematic illustration of the AEMWE single cell. (b) I-V curves for the AEMWE single cell with different MEA configurations. (c) Contact angle measurements for IrO_2-Ni_2P and IrO_2/CP. (d,e) Overpotential analysis and (f) chronopotentiometry curves for the IrO_2-Ni_2P || Pt/C/CP and IrO_2/CP || Pt/C/CP systems.

conventional powder noble-metal-based catalysts and to realize a highly efficient practical system.

3 | Conclusion

In this work, we demonstrated a polymeric binder-free approach for constructing IrO_2-Ni-based electrodes with ultralow Ir loading (<0.02 mg_{Ir} cm^{-2}) that achieved both high catalytic activity and robust stability toward the OER. Among the investigated supports, Ni_2P was identified as the most effective by providing strong interfacial coupling with IrO_2 that optimized electron density, inducing a downshift of the Ir d-band center, and moderating the binding strength of key reaction intermediates. DFT calculations corroborated these findings, revealing that the IrO_2-Ni_2P configuration exhibited the lowest free-energy barrier for OER and the most stable interfacial bonding environment. These favorable physicochemical interactions led to outstanding electrochemical performance. The IrO_2-Ni_2P electrode delivered remarkable activity (232 mV @ 10 mA cm^{-2}) in half-cell OER test and achieved 3.1 A cm^{-2} at 2.0 V_{cell} with stable operation under high-current density conditions when integrated into an AEMWE. The binder-free IrO_2-Ni_2P system also demonstrated superior mass transport, reduced ohmic losses, and preserved hydrophilicity compared to a polymeric binder-containing Ir-based standard electrode, underscoring the crucial role of support selection and electrode architecture in overcoming the intrinsic limitations of the latter. Overall, this study not only establishes IrO_2-Ni_2P as a promising anode for high-performance AEMWEs but also presents a generalizable design principle for engineering durable and efficient Ir-based OER catalysts. The integration of rational support engineering with binder-free fabrication offers a viable pathway toward reducing noble-metal usage while achieving the performance metrics required for practical large-scale water electrolyzers.

4 | Experimental Section

4.1 | Chemicals and Materials

Ni foam (thickness: 0.08 mm) was purchased from MTI Korea. Oleylamine (OLAM; technical grade, 70%), 1-octadecne (ODE; technical grade, 90%), and di-*tert*-butyl disulfide (TBDS, 97%), Nafion 117 solution (~5% in a mixture of lower aliphatic alcohols and water) were obtained from Sigma-Aldrich. Triphenyl phosphite (TPP; 97%), iridium (III) chloride hydrate ($IrCl_3.xH_2O$; 99.8%), and IrO_2 (Premion, 99.99%) were purchased from Thermo Fisher Scientific. Sodium hydroxide (NaOH; powder, 97%) and hydrochloric acid (HCl; 35–37%) were purchased from Daejung Chemicals. Commercial Pt/C on carbon paper (CP) (Pt/C/CP; 20 wt.% Pt/C, Pt loading: 0.5 mg cm^{-2}) and IrO_2 on CP (IrO_2/CP; IrO_2 loading: 3.0 mg cm^{-2}) were purchased from Fuel Cell Earth and Dioxide Materials, respectively. All chemicals were used as received without further purification.

4.2 | Synthesis of Ni-Based Foam

Before use, Ni foam (1 cm × 1.5 cm, 3 pieces) was soaked in 1 M HCl and sonicated for 15 min to eliminate the surface oxide layer. Afterward, the Ni foams were thoroughly rinsed with deionized (DI) water and ethanol at least 3 times each to ensure that the Ni foam surface was clean, followed by vacuum drying. To synthesize Ni_3S_2 foam, the pre-treated Ni foam, 10 mL OLAM, 10 mL ODE, and an equivalent molar amount of TBDS relative to Ni were placed in a three-neck flask. The solution was degassed under gentle stirring for 30 min to remove volatile impurities and subsequently purged with N_2. The solution was then heated to 190°C and maintained at this temperature for 20 min to synthesize Ni_3S_2 on Ni foam. After naturally cooling the solution to room temperature, the Ni_3S_2 foam was collected from the flask

16136829, 0, Downloaded from https://onlinelibrary.wiley.com/doi/10.1002/smll.74025 by Chung-Ang Library - Chung-Ang University , Wiley Online Library on [24/06/2026]. See the Terms and Conditions (https://onlinelibrary.wiley.com/terms-and-conditions) on Wiley Online Library for rules of use; OA articles are governed by the applicable Creative Commons License

and thoroughly rinsed several times with hexane and ethanol. The resulting Ni_3S_2 foam was vacuum-dried and annealed at 450°C for 1 h under a 4% H_2/Ar atmosphere to remove residual organic molecules. The process to fabricate the Ni_2P foam was similar except that 2.7 mL TPP was used instead of TBDS, and the reaction conditions were adjusted to 300°C for 2 h.

4.3 | IrO_2 Deposition on the Ni, Ni_3S_2, and Ni_2P Foams

For each of the foams, Ir precursor (corresponding to 0.1 mol% of Ni) was dissolved in 20 mL of 0.1 M NaOH, and the homogeneous solution was then heated to 80°C. Once the target temperature had stabilized, the as-prepared Ni-based foams were immersed in the solution and kept for 2 h. Afterward, the samples were removed from the solution, sufficiently washed with DI water, and dried under a vacuum. The detailed formation mechanism of IrO_2 on Ni-based foam is proposed in *Supplementary Note 1*.

For comparison, a commercial IrO_2-deposited Ni_2P electrode (denoted as Com. IrO_2-Ni_2P) was prepared by drop-casting IrO_2 catalyst ink onto a piece of Ni_2P foam. Specifically, 5 mg of commercial IrO_2 powder was dispersed in a solution containing 100 µL of Nafion, 490 µL of DI water, and 4.41 mL of ethanol (volume ratio = 20:480:500). The mixture was then sonicated for at least 1 h to ensure that the resulting solution was homogeneous. Afterward, the IrO_2 ink was drop-casted onto a 1 × 1 cm piece of Ni_2P foam to achieve the same Ir loading amount as IrO_2-Ni_2P (i.e., 0.016 mg_{Ir} cm^{-2}). The resulting Com. IrO_2-Ni_2P electrode was naturally dried for 12 h prior to use.

4.4 | Material Characterization

XRD analysis was conducted using a Bruker AXS New D8 Advance diffractometer equipped with a Cu Kα radiation source and a LynxEye line detector. HRTEM, STEM, and EDS mapping were performed using a field-emission transmission electron microscope (JEM–F200, JEOL, Tokyo, Japan) operating at an accelerating voltage of 200 kV. SEM and EDS analyses were carried out with a Carl Zeiss SIGMA 300 microscope (Carl Zeiss, Oberkochen, Germany). The Ir-loading amount was determined via ICP-MS (NexION 350D, PerkinElmer, USA). XPS was conducted using a K-alpha+ system (Thermo Fisher Scientific) with an Al Kα radiation source to examine the surface chemical states of the nanoparticles. The XPS spectra were calibrated by referencing the C—C peak in the C 1s region to a binding energy of 284.8 eV. A contact-angle-measuring device (DSA100S, KRÜSS) was used to measure the water contact angles on the electrodes. Raman spectra were collected using a commercial micro-Raman spectrometer (XperRam 200, Nanobase) equipped with a 532 nm laser (1 mW) and a 5× objective.

4.5 | Electrochemical Characterization

All electrochemical measurements were conducted using a three-electrode system, with the catalyst electrode as the working electrode (1 × 1 cm^2), an Hg/HgO electrode as the reference electrode, and Pt wire as the counter electrode in a 1 M KOH solution as the electrolyte. The potential was converted to the reversible hydrogen electrode (RHE) scale using the relation $E_{RHE} = E_{Hg/HgO} + 0.927$ V in 1 M KOH (pH = 14).

Alkaline OER activity was evaluated by using linear sweep voltammetry (LSV) over the potential range of 0 to 0.9 V (vs. Hg/HgO) at a scan rate of 5 mV s^{-1}. All reported OER polarization curves correspond to the reverse scan to ensure accurate evaluation of intrinsic catalytic activity. EIS was carried out at 0.58 V (vs. Hg/HgO) with an AC signal amplitude of 10 mV over a frequency range of 100 kHz to 0.1 Hz. Ohmic resistance (R_s) was obtained from Nyquist plots and used to compensate for ohmic losses in all of the polarization curves. To determine the C_{dl}, CV was conducted in the potential range of –0.1 to 0.1 V (vs. Hg/HgO) at various scan rates (40, 60, 80, 100, 120, 160, and 200 mV s^{-1}). ADT was performed using 2,000 cycles of CV within the potential range of 0 to 0.9 V (vs. Hg/HgO) at a scan rate of 100 mV s^{-1}. Chronopotentiometry measurements were carried out under both sequentially varying current densities (20, 50, 100, 50, and 20 mA cm^{-2}) and a constant current density of 10 mA cm^{-2}.

An AEMWE single cell was constructed by integrating MEA, bipolar plates, current distributors, and end plates. The MEA was designed by sandwiching the anion exchange membrane (AEM (PiperION, 20 µm) between the cathode (commercial Pt/C/CP) and anode (IrO_2-Ni_2P or IrO_2/CP): IrO_2/CP was used as a commercial reference anode. To ensure proper sealing and spacing, a 150 µm-thick gasket was used on the cathode side, while 160 and 245 µm-thick gaskets were employed for the IrO_2-Ni_2P and IrO_2/CP anode, respectively. The single cell was operated at 80°C with the 1.0 M KOH solution preheated to 80°C and supplied to the anode and cathode at flow rates of 20- and 2-mL min^{-1}, respectively. Current-voltage (I-V) curves were obtained in the voltage range of 1.0–2.0 V_{cell}, and Chronopotentiometry test was conducted at a current density of 1 A cm^{-2} for 12 h to evaluate the stability. EIS analysis was carried out across a current density range of 0.05–2 A cm^{-2} to determine the R_{ohm} of the AEMWE single cell.

4.6 | Computational Details

All DFT calculations in this study were conducted using the Vienna Ab initio Simulation Package (VASP) [65–68]. The Perdew–Burke–Ernzerhof (PBE) generalized gradient approximation (GGA) was applied for the exchange–correlation functional, and the projector augmented wave (PAW) method was employed to model core electrons [65, 69–71]. In consideration of both convergence and computational efficiency, the plane-wave energy cutoff was set to 400 eV. Electronic structure optimization was performed until the total energy change in the self-consistent field (SCF) cycle was less than 10^{-5} eV, while structural optimization proceeded until the residual force was below 0.05 eV/Å.

Slab models of Ni_2P (3 × 3 × 1), Ni_3S_2 (3 × 3 × 1), Ni (4 × 4 × 1), and IrO_2 (1 × 1 × 1) were constructed, with the in-plane cell size adjusted to ensure the surface areas of the supports were as similar as possible. A vacuum layer of 30 Å was applied to all models, and IrO_2 was positioned on the Ni, Ni_2P, and Ni_3S_2 supports in an island configuration. The Brillouin zone

16136829, 0, Downloaded from https://onlinelibrary.wiley.com/doi/10.1002/smll.74025 by Chung-Ang Library - Chung-Ang University , Wiley Online Library on [24/06/2026]. See the Terms and Conditions (https://onlinelibrary.wiley.com/terms-and-conditions) on Wiley Online Library for rules of use; OA articles are governed by the applicable Creative Commons License

was sampled using a 1 × 1 × 1 Monkhorst–Pack *k*-point grid to minimize interactions between periodic images. Based on this computational setup, the OER pathway under alkaline conditions was defined as follows:

$$4OH^- \rightarrow O_2\,(g) + 2H_2O\,(l) + 4e^-$$

This reaction proceeds through the following four electron transfer steps [72]:

$$* + OH^- \rightarrow * OH + e^-$$

$$* OH + OH^- \rightarrow * O + H_2O\,(l) + e^-$$

$$* O + OH^- \rightarrow * OOH + e^-$$

$$* OOH + OH^- \rightarrow * + O_2\,(g) + H_2O\,(l) + e^-$$

To compare the Gibbs free energy of each step, the stoichiometry of the reactants and products was adjusted as follows:

$$* + 4OH^- \rightarrow * OH + 3OH^-$$

$$* OH + 3OH^- \rightarrow * O + H_2O\,(l) + 2OH^-$$

$$* O + H_2O\,(l) + 2OH^- \rightarrow * OOH + H_2O\,(l) + OH^-$$

$$* OOH + H_2O\,(l) + OH^- \rightarrow * + O_2\,(g) + 2H_2O\,(l)$$

The Gibbs free energy for each step was calculated using the following equation:

$$\Delta G = E_{DFT} + \sum (\int dH + dZPE - TdS) - neU = E_{DFT} + \sum \left(\int C_p dT + dZPE - TdS\right) - neU$$

where E_{DFT} represents the energy obtained from DFT calculations, H is the enthalpy, ZPE is the zero-point energy, T is the temperature (300 K), S is the vibrational entropy, C_p is the heat capacity, U denotes the external bias, and the term neU refers to the product of the electron transfer number (n) and the applied potential (U).

Since this calculation was performed at a potential of 0 V vs. RHE (based on the Computational Hydrogen Electrode (CHE) model), there is a difference with the thermodynamic equilibrium potential (1.23 V) of the actual OER. Therefore, a potential correction of $U = 1.23$ V was applied, thereby enabling alignment of the computational results with the experimental conditions and the subsequent calculation of the catalyst overpotential [73].

The Gibbs free energy of OH^- was calculated using the CHE model proposed by Nørskov et al. [73] based on the following relationship:

$$\mu_{H^+} + \mu_{e^-} = \frac{1}{2} G\,(H_2)$$

Using this relationship, the Gibbs free energy of OH^- can be efficiently determined from the Gibbs free energy values of H_2 and H_2O.

The thermodynamic overpotential (η), a key indicator for evaluating catalyst activity, is calculated as follows:

$$\eta = \frac{\Delta G_{max}}{e} - 1.23V$$

where ΔG_{max} represents the largest Gibbs free-energy change among the four OER steps, and 1.23 V is the equilibrium potential for the OER under standard conditions. A smaller η value indicates better catalytic performance, and an ideal catalyst has $\eta = 0$ V [74].

Acknowledgements

This work was supported by the National Research Foundation of Korea (NRF) grants funded by the Korean government (MSIT) (grant numbers: RS-2020-NR049537, RS-2025-02309471, and RS-2025-02217649).

Conflicts of Interest

The author declares no conflicts of interest.

Data Availability Statement

The data that supports the findings of this study are available in the supplementary material of this article.

References

1. J. Zhang, X. Fu, S. Kwon, et al., "Tantalum-Stabilized Ruthenium Oxide Electrocatalysts For Industrial Water Electrolysis," *Science* 387, no. 6729 (2025): 48–55, https://doi.org/10.1126/science.ado9938.

2. Q. Liu, B. Li, C. Peng, et al., "Tailoring Pyrochlore Electrocatalyst via Bias-Induced Enhancement for Acidic Oxygen Evolution," *Advanced Energy Materials* 15, no. 32 (2025): 2501404, https://doi.org/10.1002/aenm.202501404.

3. J. Li, D. Miao, X. Guo, D. Luo, J. Ren, and Z. Chen, "Sustainable Zinc–Air Batteries: Innovations, Challenges, and Pathways to Commercialization," *Small* 21, no. 49 (2025), 08482, https://doi.org/10.1002/smll.202508482.

4. Y. Park, H. Y. Jang, T. K. Lee, et al., "Atomic-level Ru-Ir mixing in rutile-type $(RuIr)O_2$ for efficient and durable oxygen evolution catalysis," *Nature Communications* 16, no. 1 (2025): 579, https://doi.org/10.1038/s41467-025-55910-1.

5. Y. Lun, H. Chen, K. Wang, S. Song, and Y. Wang, "Discovery of Efficient Acidic Oxygen Evolution Electrocatalyst: High-Throughput Computational Screening of MgIrRu Oxide," *Advanced Energy Materials* 15, no. 29 (2025): 2405657, https://doi.org/10.1002/aenm.202405657.

6. D.-H. Ha, M. A. Islam, and R. D. Robinson, "Binder-Free and Carbon-Free Nanoparticle Batteries: A Method for Nanoparticle Electrodes without Polymeric Binders or Carbon Black," *Nano Letters* 12, no. 10 (2012): 5122–5130, https://doi.org/10.1021/nl3019559.

7. Y. Park, B. An, H. Kim, et al., "Ionomer-free Co-Ru Based Electrode For Efficient Proton Exchange Membrane Water Electrolysis Via Synergistic

16136829, 0, Downloaded from https://onlinelibrary.wiley.com/doi/10.1002/smll.74025 by Chung-Ang Library - Chung-Ang University , Wiley Online Library on [24/06/2026]. See the Terms and Conditions (https://onlinelibrary.wiley.com/terms-and-conditions) on Wiley Online Library for rules of use; OA articles are governed by the applicable Creative Commons License

Catalysis," *Chemical Engineering Journal* 511 (2025): 161979, https://doi.org/10.1016/j.cej.2025.161979.

8. D. F. Silva, F. Claudel, V. Martin, et al., "Oxygen Evolution Reaction Activity and Stability Benchmarks for Supported and Unsupported IrO x Electrocatalysts," *ACS Catalysis* 11, no. 7 (2021): 4107–4116, https://doi.org/10.1021/acscatal.0c04613.

9. S.-H. Bae, J.-E. Kim, H. Randriamahazaka, S.-Y. Moon, J.-Y. Park, and I.-K. Oh, "Seamlessly Conductive 3D Nanoarchitecture of Core–Shell Ni-Co Nanowire Network for Highly Efficient Oxygen Evolution," *Advanced Energy Materials* 7, no. 1 (2017): 1601492, https://doi.org/10.1002/aenm.201601492.

10. P. Lettenmeier, S. Kolb, N. Sata, et al., "Comprehensive Investigation Of Novel Pore-Graded Gas Diffusion Layers For High-Performance And Cost-Effective Proton Exchange Membrane Electrolyzers," *Energy & Environmental Science* 10, no. 12 (2017): 2521–2533, https://doi.org/10.1039/C7EE01240C.

11. Y. Qin, Y. Wang, R. Wen, L. Wang, M. Dou, and F. Wang, "Interface-Engineering Strategy for Boosting Low-Ir Catalytic Water Oxidation Using a Conductive Ti_4O_7 Support," *ACS Catalysis* 14 (2024): 13915–13926, https://doi.org/10.1021/acscatal.4c03862.

12. E. Oakton, D. Lebedev, M. Povia, et al., "IrO_2 -TiO_2: A High-Surface-Area, Active, and Stable Electrocatalyst for the Oxygen Evolution Reaction," *ACS Catalysis* 7, no. 4 (2017): 2346–2352, https://doi.org/10.1021/acscatal.6b03246.

13. M. Xu, M. Peng, H. Tang, W. Zhou, B. Qiao, and D. Ma, "Renaissance of Strong Metal–Support Interactions," *Journal of the American Chemical Society* 146, no. 4 (2024): 2290–2307, https://doi.org/10.1021/jacs.3c09102.

14. F. Cai, R. A, A. Kumar, Y. Sun, X. Yong, and J. Pan, "Strong Metal-Support Interaction Between Atomically Dispersed Iridium in Cobalt Phosphide for Efficient Mass/Charge Transfer Synergistically Boosts Overall Water Splitting," *Small* 21 (2025): 06936, https://doi.org/10.1002/smll.202506936.

15. T. W. van Deelen, H. Mejía, and K. P. de Jong, "Control Of Metal-Support Interactions In Heterogeneous Catalysts To Enhance Activity And Selectivity," *Nature Catalysis* 2 (2019): 955–970, https://doi.org/10.1038/s41929-019-0364-x.

16. Z. Luo, G. Zhao, H. Pan, and W. Sun, "Strong Metal–Support Interaction in Heterogeneous Catalysts," *Advanced Energy Materials* 12, no. 37 (2022): 2201395, https://doi.org/10.1002/aenm.202201395.

17. I. S. Filimonenkov, C. Bouillet, G. Kéranguéven, P. A. Simonov, G. A. Tsirlina, and E. R. Savinova, "Carbon Materials as Additives to the OER Catalysts: RRDE Study of Carbon Corrosion at High Anodic Potentials," *Electrochimica Acta* 321 (2019): 134657, https://doi.org/10.1016/j.electacta.2019.134657.

18. H.-S. Oh, H. N. Nong, T. Reier, et al., "Electrochemical Catalyst–Support Effects and Their Stabilizing Role for IrO x Nanoparticle Catalysts during the Oxygen Evolution Reaction," *Journal of the American Chemical Society* 138, no. 38 (2016): 12552–12563, https://doi.org/10.1021/jacs.6b07199.

19. D. Miao, J. Li, J. Ren, and Z. Chen, "Exploring the Potential of Ni-Based Hydrogen Evolution Catalysts in Anion Exchange Membrane Water Electrolyzer," *Advanced Materials* 38, no. 10 (2026): 20491, https://doi.org/10.1002/adma.202520491.

20. T. Kou, S. Wang, J. L. Hauser, et al., "Ni Foam-Supported Fe-Doped β-$Ni(OH)_2$ Nanosheets Show Ultralow Overpotential for Oxygen Evolution Reaction," *ACS Energy Letters* 4 (2019): 622–628, https://doi.org/10.1021/acsenergylett.9b00047.

21. L. Zhang, H. Wei, R. Yuan, P. Li, and J.-T. Ren, "Interface Engineering Of Transition-Metal-Based Electrocatalysts For Alkaline Water Splitting," *Coordination Chemistry Reviews* 545 (2025): 217009, https://doi.org/10.1016/j.ccr.2025.217009.

22. Y. Lee, S. Choi, S. Jang, et al., "Colloidal Phase Control of Ni–P Nanocrystals Reveals a P-Site Hydrogen Evolution Reaction Mechanism Distinct From Ni-rich Analogues," *Journal of Materials Chemistry A* 14, no. 2 (2026): 988–1000, https://doi.org/10.1039/D5TA06219E.

23. R. V. Genova-Koleva, F. Alcaide, G. Álvarez, et al., "Supporting IrO_2 and IrRuO nanoparticles on TiO_2 and Nb-doped TiO_2 Nanotubes As Electrocatalysts For The Oxygen Evolution Reaction," *Journal of Energy Chemistry* 34 (2019): 227–239, https://doi.org/10.1016/j.jechem.2019.03.008.

24. X. Li, Z. Gu, J. Cheng, et al., "Ir-RuOx Nanoparticles on WO_3 Ultrafine Nanowires As Catalysts for the Oxygen Evolution Reaction in Acidic Media," *ACS Applied Nano Materials* 7, no. 11 (2024): 12958–12969, https://doi.org/10.1021/acsanm.4c01516.

25. X. Zheng, M. Qin, S. Ma, et al., "Strong Oxide-Support Interaction over IrO_2 /V_2O_5 for Efficient pH-Universal Water Splitting," *Advanced Science* 9, no. 11 (2022): 2104636, https://doi.org/10.1002/advs.202104636.

26. E. Hwang, M. Kim, W. Lee, et al., "Cation-Exchange-Induced Structural And Chemical Modulation Of Transition Metal Spinel Sulfides To Enhance Their Oxygen Evolution Performance," *Chemical Engineering Journal* 494 (2024): 152903, https://doi.org/10.1016/j.cej.2024.152903.

27. Y. Lee, W. Jeong, Y. J. Hwang, et al., "Basics, Developments, And Strategies Of Transition Metal Phosphides Toward Electrocatalytic Water Splitting: Beyond Noble Metal Catalysts," *Journal of Materials Chemistry A* 12, no. 42 (2024): 28574–28594, https://doi.org/10.1039/D4TA04455J.

28. D. Wu, B. Liu, R. Li, et al., "Fe-Regulated Amorphous-Crystal Ni(Fe)P_2 Nanosheets Coupled with Ru Powerfully Drive Seawater Splitting at Large Current Density," *Small* 19, no. 36 (2023): 2300030, https://doi.org/10.1002/smll.202300030.

29. W. Li, J. Lv, X. Chen, B. Wang, and L. Wang, "Support-Accelerated Proton Transfer for Enhanced Oxygen Evolution Catalysis," *Journal of the American Chemical Society* 147, no. 32 (2025): 29505–29516, https://doi.org/10.1021/jacs.5c10092.

30. Y. Zhao, M. Zhao, X. Ding, et al., "One-Step Colloid Fabrication Of Nickel Phosphides Nanoplate/Nickel Foam Hybrid Electrode For High-Performance Asymmetric Supercapacitors," *Chemical Engineering Journal* 373 (2019): 1132–1143, https://doi.org/10.1016/j.cej.2019.05.098.

31. L. Zhang, Q. Xu, R. Zhao, Y. Hu, H. Jiang, and C. Li, "Fe-doped and sulfur-enriched Ni_3S_2 Nanowires With Enhanced Reaction Kinetics For Boosting Water Oxidation," *Green Chemical Engineering* 3, no. 4 (2022): 367–373, https://doi.org/10.1016/j.gce.2021.12.012.

32. H. Jeong, Y. Park, Y. Lee, et al., "High-Entropy CoNiFeCuP Nanoparticles As Efficient And Durable Catalysts For Alkaline Oxygen Evolution Reaction," *Journal of Materials Chemistry A* 13, no. 22 (2025): 16995–17005, https://doi.org/10.1039/D5TA01149C.

33. Y. S. Huang, S. S. Lin, C. R. Huang, M. C. Lee, T. E. Dann, and F. Z. Chien, "Raman spectrum of IrO_2," *Solid State Communications* 70 (1989): 517–522, https://doi.org/10.1016/0038-1098(89)90942-3.

34. T. Matthews, M. P. Chabalala, S. P. Mbokazi, et al., "Improving the Electrocatalytic Activity of Pd Nanoparticles Through Electronic Coupling Interaction with a Ni_2 P–MoS_2 hybrid support for ethanol electro-oxidation in an alkaline medium," *Sustainable Energy & Fuels* 9, no. 6 (2025): 1552–1564, https://doi.org/10.1039/D4SE01223B.

35. S. Madadkhani, S. Nandy, K. H. Chae, P. Aleshkevych, and M. M. Najafpour, "Unveiling the Changes of Dinickel Phosphide (Ni_2 P) in Hydrogen Evolution Reaction: Toward a Deeper Mechanistic Understanding," *ACS Applied Energy Materials* 7, no. 8 (2024): 3157–3165, https://doi.org/10.1021/acsaem.3c03145.

36. Z. Cheng, H. Abernathy, and M. Liu, "Raman Spectroscopy of Nickel Sulfide Ni_3S_2," *The Journal of Physical Chemistry C* 111, no. 49 (2007): 17997–18000, https://doi.org/10.1021/jp0770209.

37. Y. Qiu, Y. Yang, X. Wang, et al., "In Situ Raman Spectroscopic Quantification Of Aqueous Sulfate: Experimental Calibration And Application To Natural Fluid Inclusions," *Chemical Geology* 533 (2020): 119447, https://doi.org/10.1016/j.chemgeo.2019.119447.

16136829, 0, Downloaded from https://onlinelibrary.wiley.com/doi/10.1002/smll.74025 by Chung-Ang Library - Chung-Ang University , Wiley Online Library on [24/06/2026]. See the Terms and Conditions (https://onlinelibrary.wiley.com/terms-and-conditions) on Wiley Online Library for rules of use; OA articles are governed by the applicable Creative Commons License

38. W. Huo, X. Zhou, Y. Jin, et al., "Rhenium Suppresses Iridium (IV) Oxide Crystallization and Enables Efficient, Stable Electrochemical Water Oxidation," *Small* 19, no. 19 (2023): 2207847, https://doi.org/10.1002/smll.202207847.

39. J. Cao, T. Mou, B. Mei, et al., "Improved Electrocatalytic Activity and Stability by Single Iridium Atoms on Iron-based Layered Double Hydroxides for Oxygen Evolution," *Angewandte Chemie International Edition* 62, no. 43 (2023): 202310973, https://doi.org/10.1002/anie.202310973.

40. Y. Hu, T. Shen, Z. Song, et al., "Atomic Modulation of Single Dispersed Ir Species on Self-Supported NiFe Layered Double Hydroxides for Efficient Electrocatalytic Overall Water Splitting," *ACS Catalysis* 13, no. 16 (2023): 11195–11203, https://doi.org/10.1021/acscatal.3c02628.

41. M. Kim, H. Kang, E. Hwang, et al., "Facile Colloidal Synthesis of Transition Metal (Co, Fe, and Ni)-Added Ir-W NPs for HER in Acidic Electrolyte," *Applied Surface Science* 612 (2023): 155862, https://doi.org/10.1016/j.apsusc.2022.155862.

42. V. Pfeifer, T. E. Jones, J. J. Velasco Vélez, et al., "The Electronic Structure Of Iridium And Its Oxides," *Surface and Interface Analysis* 48, no. 5 (2016): 261–273, https://doi.org/10.1002/sia.5895.

43. Z. Chen, Y. Song, J. Cai, et al., "Tailoring the d-Band Centers Enables Co_4N Nanosheets To Be Highly Active for Hydrogen Evolution Catalysis," *Angewandte Chemie International Edition* 57, no. 18 (2018): 5076–5080, https://doi.org/10.1002/anie.201801834.

44. S. Niu, X.-P. Kong, S. Li, et al., "Low Ru loading RuO_2/$(Co,Mn)3O_4$ Nanocomposite With Modulated Electronic Structure For Efficient Oxygen Evolution Reaction In Acid," *Applied Catalysis B: Environmental* 297 (2021): 120442, https://doi.org/10.1016/j.apcatb.2021.120442.

45. Y. Wang, Y. Qin, R. Wen, L. Wang, M. Dou, and F. Wang, "High-Performance Low-Iridium Catalyst for Water Oxidation: Breaking Long-Ranged Order of IrO_2 by Neodymium Doping," *Small* 20, no. 42 (2024): 2401964, https://doi.org/10.1002/smll.202401964.

46. S. Ke, L. Qiu, W. Zhao, et al., "Understanding of Correlation between Electronic Properties and Sulfur Tolerance of Pt-Based Catalysts for Hydrogen Oxidation," *ACS Applied Materials & Interfaces* 14, no. 6 (2022): 7768–7778, https://doi.org/10.1021/acsami.1c18905.

47. Q. Quan, Y. Zhang, H. Li, et al., "Atomic-Scale Self-Rearrangement Of Hetero-Metastable Phases Into High-Density Single-Atom Catalysts For The Oxygen Evolution Reaction," *Nature Communications* 16, no. 1 (2025): 2908, https://doi.org/10.1038/s41467-025-58163-0.

48. O. Kasian, J.-P. Grote, S. Geiger, S. Cherevko, and K. J. J. Mayrhofer, "The Common Intermediates of Oxygen Evolution and Dissolution Reactions during Water Electrolysis on Iridium," *Angewandte Chemie International Edition* 57, no. 9 (2018): 2488–2491, https://doi.org/10.1002/anie.201709652.

49. S. Sankar, Y. Sugawara, S. Assa Aravindh, et al., "Tuning Palladium Nickel Phosphide toward Efficient Oxygen Evolution Performance," *ACS Applied Energy Materials* 3, no. 1 (2020): 879–888, https://doi.org/10.1021/acsaem.9b01996.

50. D. Li, W. Wan, Z. Wang, et al., "Self-Derivation and Surface Reconstruction of Fe-Doped Ni_3S_2 Electrode Realizing High-Efficient and Stable Overall Water and Urea Electrolysis," *Advanced Energy Materials* 12, no. 39 (2022): 2201913, https://doi.org/10.1002/aenm.202201913.

51. S. J. Freakley, J. Ruiz-Esquius, and D. J. Morgan, "The X-ray Photoelectron Spectra of Ir, IrO_2 and $IrCl_3$ Revisited," *Surface and Interface Analysis* 49, no. 8 (2017): 794–799, https://doi.org/10.1002/sia.6225.

52. K.-R. Yeo, K.-S. Lee, H. Kim, J. Lee, and S.-K. Kim, "A Highly Active and Stable 3D Dandelion Spore-Structured Self-Supporting Ir-Based Electrocatalyst For Proton Exchange Membrane Water Electrolysis Fabricated Using Structural Reconstruction," *Energy & Environmental Science* 15, no. 8 (2022): 3449–3461, https://doi.org/10.1039/D2EE01042A.

53. Y. Pan, Y. Liu, J. Zhao, et al., "Monodispersed Nickel Phosphide Nanocrystals With Different Phases: Synthesis, Characterization And Electrocatalytic Properties For Hydrogen Evolution," *Journal of Materials Chemistry A* 3, no. 4 (2015): 1656–1665, https://doi.org/10.1039/C4TA04867A.

54. C. Huang and P. K. Chu, "Recommended practices and benchmarking of foam electrodes in water splitting," *Trends in Chemistry* 4 (2022): 1065–1077, https://doi.org/10.1016/j.trechm.2022.09.008.

55. X. Du, Y. Sun, J. Cui, et al., "Covalency Regulation of Ru-Based Solid Solutions by Iridium for Durable Proton Exchange Membrane Water Electrolysis at 2 A cm^{-2}," *Advanced Functional Materials* 35 (2025): 2506203, https://doi.org/10.1002/adfm.202506203.

56. X. Wang, W. Pi, Z. Li, et al., "Orbital-Level Band Gap Engineering of RuO_2 for Enhanced Acidic Water Oxidation," *Nature Communications* 16, no. 1 (2025): 4845, https://doi.org/10.1038/s41467-025-60083-y.

57. C. Yang, Y. Zhu, F. Zhang, et al., "Sulfur-Doped IrO_2 Enable Pathway Switch to Lattice Oxygen Mechanism with Enhanced Stability for Low Iridium PEM Water Electrolysis," *Advanced Materials* 37, no. 38 (2025): 2507560, https://doi.org/10.1002/adma.202507560.

58. F. Wang, L. Feng, M. Zhang, and H. Cong, "Engineering Oxygen Nonbonding States In High Entropy Hydroxides For Scalable Water Oxidation," *Nature Communications* 16, no. 1 (2025): 6624, https://doi.org/10.1038/s41467-025-61766-2.

59. A. Zagalskaya and V. Alexandrov, "Role of Defects in the Interplay Between Adsorbate Evolving and Lattice Oxygen Mechanisms of the Oxygen Evolution Reaction in RuO_2 and IrO_2," *ACS Catalysis* 10 (2020): 3650–3657, https://doi.org/10.1021/acscatal.9b05544.

60. S. Liu, Y. Chang, N. He, S. Zhu, L. Wang, and X. Liu, "Competition between Lattice Oxygen and Adsorbate Evolving Mechanisms in Rutile Ru-Based Oxide for the Oxygen Evolution Reaction," *ACS Applied Materials & Interfaces* 15, no. 16 (2023): 20563–20570, https://doi.org/10.1021/acsami.3c02086.

61. I. C. Man, H.-Y. Su, F. Calle-Vallejo, et al., "Universality in Oxygen Evolution Electrocatalysis on Oxide Surfaces," *ChemCatChem* 3, no. 7 (2011): 1159–1165, https://doi.org/10.1002/cctc.201000397.

62. R. B. Kutz, Q. Chen, H. Yang, S. D. Sajjad, Z. Liu, and I. R. Masel, "Sustainion Imidazolium-Functionalized Polymers for Carbon Dioxide Electrolysis," *Energy Technology* 5 (2017): 929–936, https://doi.org/10.1002/ente.201600636.

63. A. Angulo, P. van der Linde, H. Gardeniers, M. Modestino, and D. Fernández Rivas, "Influence of Bubbles on the Energy Conversion Efficiency of Electrochemical Reactors," *Joule* 4, no. 3 (2020): 555–579, https://doi.org/10.1016/j.joule.2020.01.005.

64. H. Oh, H. Han, J. Kim, et al., "Self-supported electrodes to enhance mass transfer for high-performance anion exchange membrane water electrolyzer," *Chemical Engineering Journal* 460 (2023): 141727, https://doi.org/10.1016/j.cej.2023.141727.

65. G. Kresse and J. Furthmüller, "Efficient iterative schemes for ab initio total-energy calculations using a plane-wave basis set," *Physical Review B* 54, no. 16 (1996): 11169–11186, https://doi.org/10.1103/PhysRevB.54.11169.

66. G. Kresse and J. Furthmüller, "Efficiency of Ab-Initio Total Energy Calculations For Metals And Semiconductors Using A Plane-Wave Basis Set," *Computational Materials Science* 6 (1996): 15–50, https://doi.org/10.1016/0927-0256(96)00008-0.

67. G. Kresse and J. Hafner, "Ab Initio Molecular-Dynamics Simulation Of The Liquid-Metal–Amorphous-Semiconductor Transition In Germanium," *Physical Review B* 49, no. 20 (1994): 14251–14269, https://doi.org/10.1103/PhysRevB.49.14251.

68. G. Kresse and J. Hafner, "Ab Initio Molecular Dynamics for Liquid Metals," *Physical Review B* 47, no. 1 (1993): 558–561, https://doi.org/10.1103/PhysRevB.47.558.

69. P. Pulay, "Convergence Acceleration Of Iterative Sequences. the Case of scf Iteration," *Chemical Physics Letters* 73, no. 2 (1980): 393–398, https://doi.org/10.1016/0009-2614(80)80396-4.

70. P. E. Blöchl, "Projector Augmented-Wave Method," *Physical Review B* 50, no. 24 (1994): 17953–17979, https://doi.org/10.1103/PhysRevB.50.17953.

16136829, 0, Downloaded from https://onlinelibrary.wiley.com/doi/10.1002/smll.74025 by Chung-Ang Library - Chung-Ang University , Wiley Online Library on [24/06/2026]. See the Terms and Conditions (https://onlinelibrary.wiley.com/terms-and-conditions) on Wiley Online Library for rules of use; OA articles are governed by the applicable Creative Commons License

71. J. P. Perdew, K. Burke, and M. Ernzerhof, "Generalized Gradient Approximation Made Simple," *Physical Review Letters* 77, no. 18 (1996): 3865–3868, https://doi.org/10.1103/PhysRevLett.77.3865.

72. Q. Liang, G. Brocks, and A. Bieberle-Hütter, "Oxygen Evolution Reaction (OER) Mechanism Under Alkaline and Acidic Conditions," *Journal of Physics: Energy* 3, no. 2 (2021): 026001, https://doi.org/10.1088/2515-7655/abdc85.

73. J. K. Nørskov, J. Rossmeisl, A. Logadottir, et al., "Origin of the Overpotential for Oxygen Reduction at a Fuel-Cell Cathode," *The Journal of Physical Chemistry B* 108, no. 46 (2004): 17886–17892, https://doi.org/10.1021/jp047349j.

74. Y. Zhang, T. Wang, L. Mei, et al., "Rational Design of Cost-Effective Metal-Doped ZrO_2 for Oxygen Evolution Reaction," *Nano-Micro Letters* 16, no. 1 (2024): 180, https://doi.org/10.1007/s40820-024-01403-7.

Supporting Information

Additional supporting information can be found online in the Supporting Information section.

Supporting File: smll74025-sup-0001-SuppMat.docx.

16136829, 0, Downloaded from https://onlinelibrary.wiley.com/doi/10.1002/smll.74025 by Chung-Ang Library - Chung-Ang University , Wiley Online Library on [24/06/2026]. See the Terms and Conditions (https://onlinelibrary.wiley.com/terms-and-conditions) on Wiley Online Library for rules of use; OA articles are governed by the applicable Creative Commons License